Tectonophysics 668–669 (2016) 1–14

Contents lists available at ScienceDirect

Tectonophysics

journal homepage: www.elsevier.com/locate/tecto

Review Article

Inferring upper-mantle flow from seismic anisotropy: An experimental perspective

Philip Skemer [a,*], Lars N. Hansen [b]

[a] Washington University in St Louis, USA
[b] Oxford University, UK

ARTICLE INFO

Article history:
Received 19 June 2015
Received in revised form 7 November 2015
Accepted 5 December 2015
Available online 22 December 2015

Keywords:
Seismic anisotropy
Mantle convection
Olivine
CPO

ABSTRACT

Patterns of mantle flow are most directly inferred from observations of seismic anisotropy, which is mainly caused by the crystallographic preferred orientation (CPO) of olivine, the most abundant mineral in the upper mantle. CPO is generated by high temperature ductile deformation, which often yields predictable relationships between the elastic or seismic properties of a material and the kinematics of flow. Over the last 15 years there has been a wealth of new data describing the how olivine CPO forms and evolves as a function of deformation conditions and strain magnitude. In this review, we explore the relationships between deformation, the evolution of CPO, and the development of seismic anisotropy, from the perspective of experimental rock mechanics. We first review the experimental basis for the study of olivine CPO evolution from the formative studies in the early nineteen sixties through recent advances. We then review some emerging complications to the study of CPO evolution, such as the long-lived transient CPOs that arise from changes in deformation kinematics, mechanisms, and conditions. Finally we discuss the origins of seismic anisotropy and the challenges of interpreting seismic anisotropy in terms of mantle flow.

Contents

1. Introduction

The flow of rocks in Earth's interior is a manifestation of mantle convection and one of the basic elements of Earth's secular evolution. In principle, knowledge of mantle flow patterns provides fundamental

* Corresponding author at: Rudolph Hall Rm 110, Washington University in Saint Louis, 1 Brookings Drive, Saint Louis, MO 63130, USA. Tel.: +1 314 935 3584.
E-mail address: pskemer@wustl.edu (P. Skemer).

http://dx.doi.org/10.1016/j.tecto.2015.12.003
0040-1951/

constraints to the thermal and chemical history of the planet and the physical processes that are the foundation of plate tectonics. The study of mantle flow has benefited from the integrated effort of scientists from disciplines spanning the earth sciences. In this review, we will provide an overview of the interpretation of mantle flow from seismological observations while highlighting the perspective provided by experimental rock deformation.

By the mid-20th century, a growing body a literature demonstrated that olivine-rich rocks often exhibit a crystallographic texture. This texture was recognized by the systematic relationship between olivine's crystallographic axes and the macroscopic foliation of the rock (Andreatta, 1934; Turner, 1942), a feature now widely described as crystallographic preferred orientation (CPO) or lattice-preferred orientation (LPO).[1] In many cases olivine grains are oriented so that the [010] crystallographic axes are clustered normal to the schistosity or compositional banding, while the [100] and [001] axes are distributed in a girdle within the foliation plane, producing a texture that is axially symmetric (Brothers, 1959). Although both igneous and metamorphic origins of these microstructures were proposed, by the 1960s it was generally concluded that most CPO was generated by plastic deformation and recrystallization under sub-solidus conditions (Christensen and Crosson, 1968; Turner and Weiss, 1963).

Around the same time, laboratory measurements began documenting the orientation dependence of seismic wave velocities in olivine (Birch, 1960, 1961; Verma, 1960). In experiments on olivine single crystals, compressional waves were shown to travel fastest parallel to [100] and slowest parallel to [010], reflecting anisotropy in excess of 24% (Verma, 1960). In polycrystalline samples of dunite and olivine-rich harzburgite similar trends were observed, with the slowest velocities recorded in orientations parallel to concentrations of [010] axes. Although the magnitude of compressional wave anisotropy is smaller in polycrystalline materials, ranging from 3–10% (Birch, 1961), the potential significance of olivine CPO as a source of anisotropy in the mantle was clear.

A major conceptual advancement, linking mantle flow, olivine CPO, and seismic anisotropy was first proposed by Hess (1964). In this seminal work, Hess discussed results by Raitt (1963) and Shor and Pollard (1964), which described azimuthal variation of horizontally propagating seismic wave velocities near the Mendicino and Molokai fracture zones in the Pacific Basin. The fastest directions of wave propagation were those parallel to the strike of the fracture zones, which was also interpreted to be the direction of mantle flow. Citing the petrofabrics described by Turner (1942) and the experimental results of Verma (1960), Hess suggested that the seismic anisotropy could be attributed to the tectonically driven shear deformation of olivine. This fundamental idea established the basis for 50 years of study on the flow patterns in Earth's mantle.

Over the last several decades two basic approaches, illustrated schematically in Fig. 1, have been used to advance the study of mantle flow. The first approach, which we will call the inverse approach, uses as its starting point seismological observations. Seismic anisotropy at the plate scale (e.g. Ekstrom and Dziewonski, 1998; Nishimura and Forsyth, 1989; Tanimoto and Anderson, 1985; Wolfe and Solomon, 1998; Yuan and Romanowicz, 2010) is related to micro-scale or continuum descriptions of CPOs, which may be derived from rock physics experiments (Bystricky et al., 2000; Jung and Karato, 2001; Nicolas et al., 1973; Zhang and Karato, 1995) geological observations (Ben Ismail and Mainprice, 1998; Christensen and Lundquist, 1982; Mercier and Nicolas, 1975; Nicolas and Christensen, 1987; Nicolas et al., 1971), or microphysical modeling (Chastel et al., 1993; Kaminski and Ribe, 2001; Ribe and Yu, 1991; Tommasi et al., 2000; Wenk and Tomé, 1999; Wenk et al., 1991). The relationship between the inferred CPO and the kinematics of rock deformation is used to constrain patterns of mantle flow in the tectonic setting of interest (Carter et al., 1972; Karato et al., 2008; Long and Silver, 2009; Mainprice and Silver, 1993; Nicolas and Christensen, 1987).

The second approach, which we will call the forward approach, uses as its starting point a numerical model for mantle flow (Becker et al., 2003, 2006, 2008; Blackman and Kendall, 2002; Castelnau et al., 2009; Conrad and Behn, 2010; Faccenda and Capitanio, 2012; Kneller et al., 2005; Tanimoto and Anderson, 1984; Tommasi, 1998). The flow model is coupled to a conceptual or numerical model for CPO evolution, parameterized through comparison with geological observations or laboratory experiments (Castelnau et al., 2008; Kaminski et al., 2004; Tommasi et al., 2000; Wenk and Tomé, 1999). The CPO generated in this manner is used to forward model mantle anisotropy using data on mineral elasticity (Baker and Carter, 1972). Comparison between the forward model and seismological observations is used to test the validity of this approach (Becker et al., 2006, 2014; Conder and Wiens, 2007; Conrad et al., 2007; Ito et al., 2015).

In both the inverse and forward approaches there are several layers of assumptions that must be made. Among the most critical are the relationships between flow and the evolution of CPO. CPO is not a simple property of materials, and varies in strength, symmetry, and orientation as a function of composition; strain magnitude, path, and geometry; stress; temperature; pressure; and deformation mechanism (e.g. Karato et al., 2008; Mainprice, 2015). Moreover, CPO may evolve slowly with progressive strain and may not be in equilibrium with the instantaneous strain field, particularly under continents and near plate boundaries (Becker et al., 2003, 2014; Boneh et al., 2015; Castelnau et al., 2009; Conrad et al., 2007; Kaminski and Ribe, 2002; Skemer et al., 2012). For these reasons the relationships among mantle flow, CPO, and seismic anisotropy are non-trivial and geodynamic interpretations must be evaluated critically.

There have been several recent reviews related to these topics. The reader is directed to Mainprice (2015) for a review of the underlying mineral physics of mantle seismic anisotropy, to Karato et al. (2008) for a discussion of the relationships between olivine fabrics and mantle geodynamics, and Long and Silver (2009) and Long and Becker (2010) for reviews of the state of understanding of mantle anisotropy. In this paper, we will focus mainly on the experimental perspective, reviewing the experimental basis for the generation of olivine CPO, with particular emphasis placed on the importance of the evolution of CPO as a function of deformation conditions. In Section 2 we review experimental studies of CPO evolution from the early nineteen sixties to the present. In Section 3 we discuss some details of CPO evolution, in particular the transient CPOs that arise from changes in deformation kinematics, mechanisms, and conditions. In Section 4 we review the origins of seismic anisotropy and discuss the specific challenges of interpreting seismic anisotropy in terms of mantle flow.

2. Experimental studies of olivine CPO

2.1. Experimental studies (1963–2000)

With the emergence of plate tectonic theory came renewed interest in the constitution and rheology of the mantle (Carter et al., 1972). Rock deformation experiments sought to understand both the rheology of plausible upper-mantle compositions and the microstructures produced by deformation. Microstructure, including CPO, is a key to relating processes observed in the lab to processes in nature. Comparison of microstructures formed in these two different environments helps to validate the extrapolation of laboratory flow laws to geologic time scales, providing a framework for interpreting seismic anisotropy.

Some of the first high-pressure and temperature deformation experiments on olivine were performed by Raleigh (1963). Detailed microstructural observation, including analysis of slip bands, deformation

[1] In geophysical literature CPO and LPO are used synonymously, although there is some regional preference in their application. As the term "lattice" is more ambiguous than "crystallographic," we have a slight preference for CPO and will use this term throughout the present review.

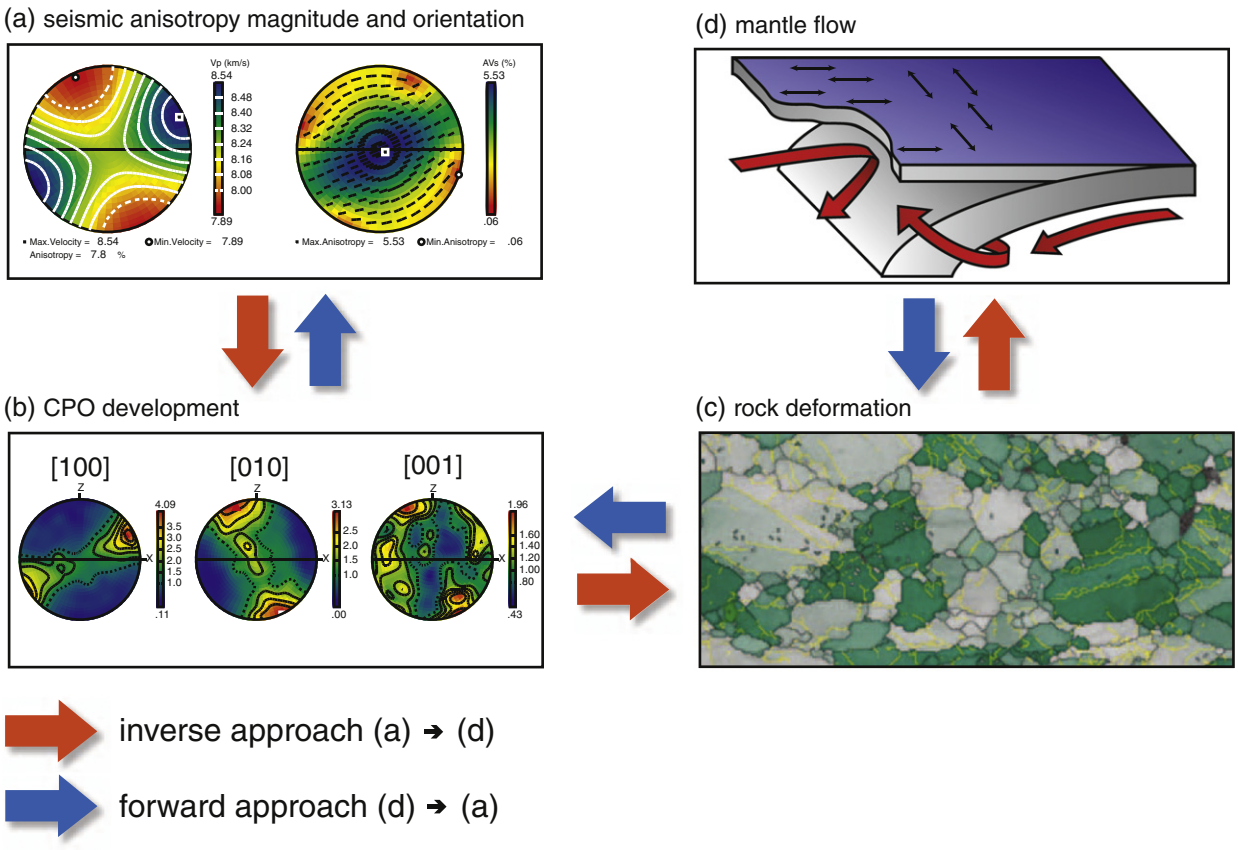

Fig. 1. Process diagram illustrating two conceptual approaches for relating rock deformation, CPO development, seismic anisotropy, and the interpretation of mantle flow. (a) Seismic anisotropy at the plate scale can be interpreted in the context of the continuous properties of minerals such as olivine. The anisotropic properties of olivine are represented here by pole figures in a kinematic reference frame. P and S-wave anisotropy are shown on the left and right, respectively. Data are from experiment PI-284 of Zhang and Karato (1995). (b) CPO is illustrated by pole figures of crystal orientation using the same reference frame and data as in (a). (c) Rock deformation is illustrated using an EBSD dataset from Hansen et al. (2011). Colors correspond to crystallographic orientation while black and yellow lines mark grain and subgrain boundaries, respectively. (d) Geodynamic and seismological data are illustrated in this cartoon after Karato et al. (2008), showing plausible paths of mantle flow in subduction zones, and some of the corresponding shear wave splitting observations. In the inverse approach (orange arrows) observations of seismic anisotropy are compared to particular CPO patterns from experiments or natural samples. These CPO patterns are used to infer deformation conditions, mechanisms, and kinematics, which are then used to interpret mantle-scale flow patterns. In the forward approach (blue arrows) numerical models are used to simulate mantle flow at the macroscopic scale. Micromechanical models of CPO evolution simulate the development of seismic anisotropy, which can then be compared with observation.

lamellae, and kink bands, led to the identification of several unique crystallographic slip-systems,[2] the relative activity of which was determined to be sensitive to both temperature and strain-rate (Raleigh, 1968). At the highest temperatures (~1000 °C), slip was inferred to occur primarily on [100]{0kl}, while at lower temperatures slip was accommodated by various slip systems with a [001] Burgers vector. Raleigh's experiments were also able to reproduce (100) tilt walls, which had been previously identified in naturally deformed samples (Raleigh, 1965). Subsequent work by Carter and Ave Lallemant (1970) built on these findings by expanding the range of deformation conditions to 1400 °C and 3 GPa confining pressure. The slip systems identified by Carter and Ave Lallemant (1970) were similar to the findings of Raleigh (1968), with the additional identification of the [100](010) system at temperatures in excess of 1100 °C.

A companion paper by Ave'Lallemant and Carter (1970) explored the significance of the deformation microstructures, concluding that olivine at mantle conditions deforms primarily by dislocation glide and climb, and syntectonic (dynamic) recrystallization. Ave'Lallemant and Carter (1970) also presented the CPOs from the associated experimental study, which were measured using a universal-stage microscope. Like most rock deformation experiments at this time, the geometry of deformation was triaxial compression (Fig. 2a). In this configuration, $\sigma_1 > \sigma_2 = \sigma_3$ where σ_1 is the maximum compressive stress and is parallel to the axis of shortening; σ_2 and σ_3 are the intermediate and minimum compressive stresses respectively, and are oriented in an axial plane that is perpendicular to σ_1. The equivalence of two principal stresses in a triaxial experiment means that grains aligned by slip do not favor any particular direction within the axial plane (Fig. 2b,c). Hence, in triaxial compression, the textures that arise from the activation of (010)[100] at high temperature are axisymmetric, with [010] point maxima parallel to the compression axis and girdles of [100] and [001] axes perpendicular to the compression axis.

A series of experiments published by Nicolas et al. (1973) corroborated the basic findings of Ave'Lallemant and Carter (1970) while investigating the additional dimension of strain. Starting from a synthetic material with an initially random CPO, a series of triaxial experiments

[2] Slip systems are defined by a slip direction and a slip plane. For dislocations moving by a glide mechanism, the slip direction is parallel to the Burgers vector. Square brackets denote crystallographic directions. Parentheses and curled brackets denote crystallographic planes and sets of crystallographic planes, respectively. We use the standard Miller index notation for crystallographic orientations. [100]{0*kl*} refers to slip in the [100] or "a" direction on a several slip planes {0*kl*}, where *k* and *l* refer to several combinations of low-index crystal orientations.

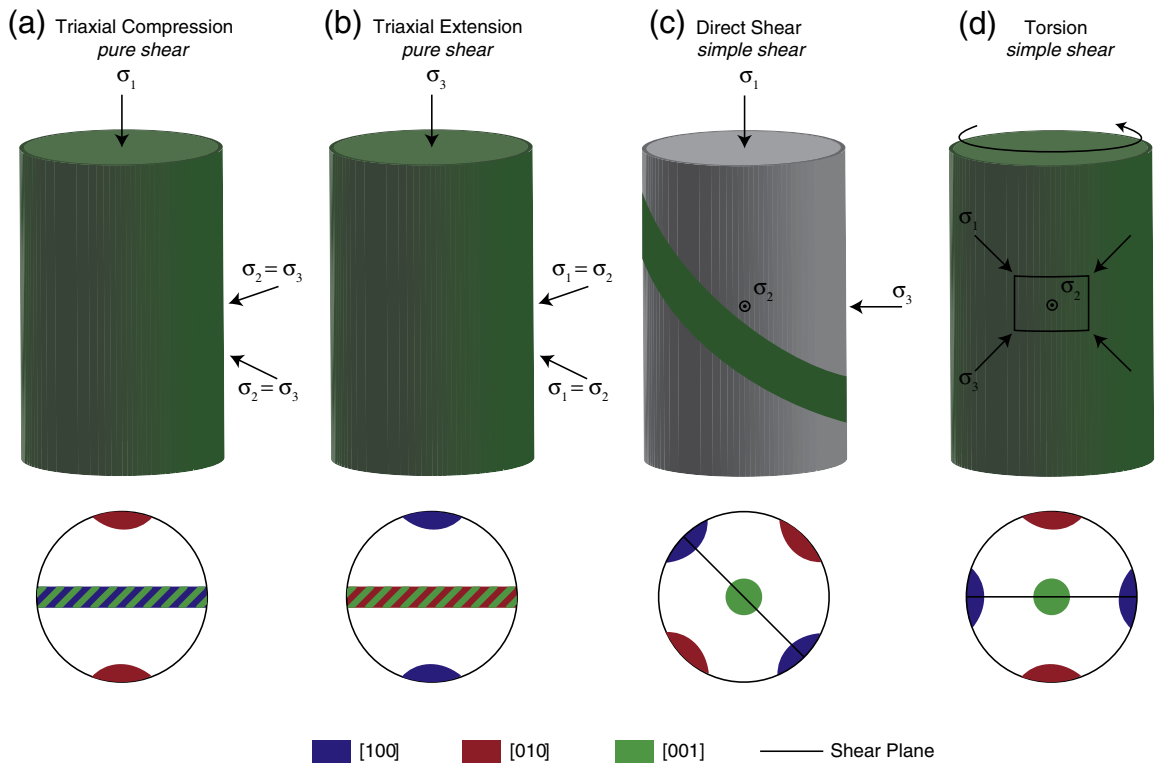

Fig. 2. Schematic diagram illustrating four common geometries for rock deformation experiments described in this review: (a) triaxial compression, (b) triaxial extension, (c) direct shear, and (d) torsion. Principal stresses are noted. In triaxial and torsion configurations samples are generally cylindrical. In direct shear experiments samples are disk shaped and sandwiched between two rigid anvils (shown in gray). Triaxial experiments typically generate CPOs that are radially symmetric, as two of the principal stresses are the same. Direct shear and torsion experiments, which are nearly simple shear, produce CPOs that are typically orthorhombic. The bottom row of pole figures shows the expected orientations of crystal axes in stereographic projection, in the same reference frame as the associated cartoons, assuming slip is mainly accommodated by the [100](010) slip system.

up to linear strains of $\varepsilon = 0.58$ demonstrated that CPO strengthens with progressive strain. While the strength of the CPO increased, the symmetry and orientation of the CPO from lower strain experiments was preserved at larger strains.

Zhang and Karato (1995) were the first to generate olivine CPOs in simple shear, using a gas medium apparatus and a direct-shear assembly (Fig. 2c). CPOs from these experiments exhibit orthorhombic symmetry, reproducing many of the observations from ophiolites, xenoliths, and alpine-style massifs (Mainprice and Silver, 1993; Ben Ismail and Mainprice, 1998; and references therein). Similarly to the observations of Nicolas et al. (1973), CPOs strengthened with progressive strain (Zhang et al., 2000). However unlike the results by Nicolas and coauthors, the CPO is observed to rotate systematically. At low strains, olivine [100] axes follow the trajectory of the major axis of the finite strain ellipse, which is initially oriented at a 45-degree angle to the shear direction. When shear strains exceed $\gamma \sim 1$, the orientation of olivine [100] axes deviates from the orientation of the finite strain ellipse and becomes aligned with the shear direction (Fig. 3). The orientation of olivine [010] axes follows a complementary path, becoming aligned with the normal to the shear plane at large strains. One notable observation from this study is that the rotation of the olivine CPO is temperature dependent. The CPO of experiments at 1300 °C becomes aligned with the shear direction at shear strains of $\gamma \sim 1$. However the CPO of experiments at 1200 °C remains oblique to the shear direction by about 20°, over the same range of strains. Along with data on the temperature dependence of slip system activity (Carter and Ave Lallemant, 1970; Raleigh, 1968), these results by Zhang and Karato (1995) indicate that CPO evolution is a temperature dependent phenomenon.

The maximum shear strain achieved in Zhang and Karato's (1995) direct shear experiments was limited to $\gamma = 1.5$. Experiments by Bystricky et al. (2000) took advantage of a newly designed Paterson apparatus with a torsional actuator (Paterson and Olgaard, 2000) (Fig. 2d) to generate shear strains in olivine up to $\gamma = 5.0$. The textures generated in this study exhibit strong clustering of [100] axes parallel to the shear direction and girdles of [010] and [001] perpendicular to the shear direction, reproducing the texture predicted by Raleigh (1968) and observed in some natural samples (texture with this symmetry is sometimes referred to as "pencil glide.") CPO in the experiments by Bystricky et al. (2000) strengthened with progressive strain, however the [100] axes remained parallel to the shear direction throughout the range of strains, and did not exhibit the progressive rotation with strain observed in the experiments of Zhang and Karato (1995) (Fig. 3).

2.2. Experimental studies (2001–present)

The last 15 years have seen rapid progress in the experimental study of CPO evolution. New rock deformation apparatus, including the torsional Paterson apparatus (Paterson and Olgaard, 2000), Rotational Drickamer Apparatus (Yamazaki and Karato, 2001), and the D-DIA apparatus (Wang et al., 2003), have expanded the range of deformation conditions that can be achieved experimentally. The commercial availability of electron backscatter diffraction (EBSD) systems has made routine the process of measuring CPO, even in highly deformed, fined-grained materials (Prior et al., 1999). During this period, a broad range of experimental studies has explored the effects of deformation conditions, including water, temperature, pressure, and stress, on slip-system activity and olivine CPO formation.

A major advancement in the recent study of mantle CPOs was the discovery that olivine can adopt several previously unrecognized CPO configurations, depending on the thermodynamic conditions of

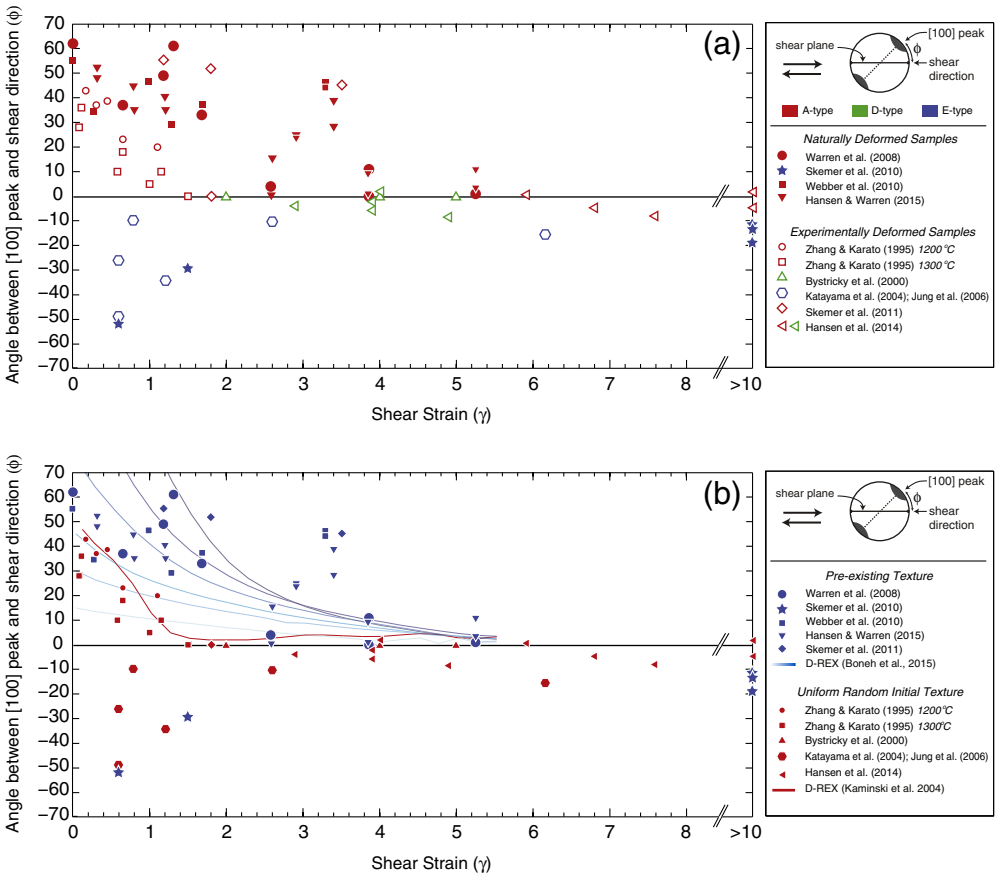

Fig. 3. The orientation of olivine [100] axes with respect to the shear plane (ϕ) as a function of shear strain (γ). Sense of shear as shown. (a) Data include experiments (open shapes) and naturally deformed samples (solid shapes). Samples interpreted in the original cited study to be A-, D-, or E-type CPOs are colored red, green, and blue, respectively. Olivine A-type and E-type CPOs evolve differently, with the E-type CPOs apparently rotating antithetically to the sense of rotation induced by simple shear. Hence there is a wide spectrum of potential angular relationships between the seismically fast direction of olivine and the kinematics of flow, which persists to large strains. (b) The same data are plotted with colors reflecting the presence (blue) or absence (red) of a pre-existing texture in the associated dataset. The D-REX model of Kaminski et al. (2004) (red line), which is parameterized through comparison with the experiments of Zhang and Karato (1995), is initiated with a random texture. A modified D-REX model (Boneh et al., 2015), which is parameterized through comparison with the experiments of Boneh and Skemer (2014), is shown as a series of blue lines. This latter set of models is initiated with a strong pre-existing A-type texture, which is rotated into several starting orientations (initial values for $\phi = 15; 30; 45; 75; 105; 135°$) to simulate two stages of deformation. Experiments, natural samples, and models are in broad agreement: even at moderate to large shear strains, there may be considerable obliquity between the orientation of the seismically fast olivine [100] axes and the direction of shear.

deformation. Jung and Karato (2001) and Katayama et al. (2004) identified three new olivine CPO types; along with the CPOs described by Zhang and Karato (1995) and Bystricky et al. (2000) these are now commonly referred to as A, B, C, D, and E-type olivine fabrics (Fig. 4). Three of the CPOs (A, D, and E-type) are characterized by [100] maxima roughly aligned with the flow direction, consistent with slip on one or more of the [100] slip systems. The other two CPOs (B- and C-type) are characterized by [001] maxima aligned with the flow direction, suggesting deformation was produced primarily by slip on a [001] slip system. E, B, and C-type CPOs were originally considered to form only at elevated water contents. However, recent experiments under dry conditions have since demonstrated that slip in the [001] direction is favored over slip in the [100] direction at high pressures, which may promote the formation of B- and C-type CPOs in the deep mantle (Couvy et al., 2004; Raterron et al., 2009). Apparent "B-type" fabrics can also be generated when melt and solid in partially molten rocks experience different deformation kinematics (Holtzman et al., 2003), or arise due to the preservation of relict fabrics from previous deformation events (Boneh et al., 2015).

Because of the distinct relationship between the olivine crystallographic axes and the kinematics of shear, each olivine CPO generates its own unique anisotropic signature (Jung et al., 2006). These CPOs have been widely cited as possible explanations for various seismological observations in the upper mantle, including observations of trench-parallel anisotropy (e.g. Long and Silver, 2009). For further details on the origins and seismological significance of these olivine fabrics the reader is referred to the review by Karato et al. (2008).

3. Transient CPOs and the evolution towards steady state

3.1. Predicted steady state CPOs

CPO is a dynamic property of materials, which evolves through a combination of deformation and recovery processes. Simple interpretations of seismic anisotropy in terms of mantle flow require the assumption, often implicit, that CPO has reached a predictable steady-state configuration and that steady state is achieved faster than the rate at which deformation conditions or kinematics are changing.

Experiments and theory predict that steady-state olivine CPO is a function of slip system activity, the geometry of deformation, and the microphysics of dynamic recrystallization (Kaminski and Ribe, 2001; Karato, 1988; Karato et al., 2008; Tommasi et al., 2000). Under most conditions, olivine CPO is observed to evolve towards a kinematic reference frame (Karato, 1987; Nicolas and Christensen, 1987) in which the dominant crystallographic slip direction is aligned with the direction of maximum extension and the dominant crystallographic slip plane is aligned perpendicularly to the direction of shortening (Fig. 4). In the

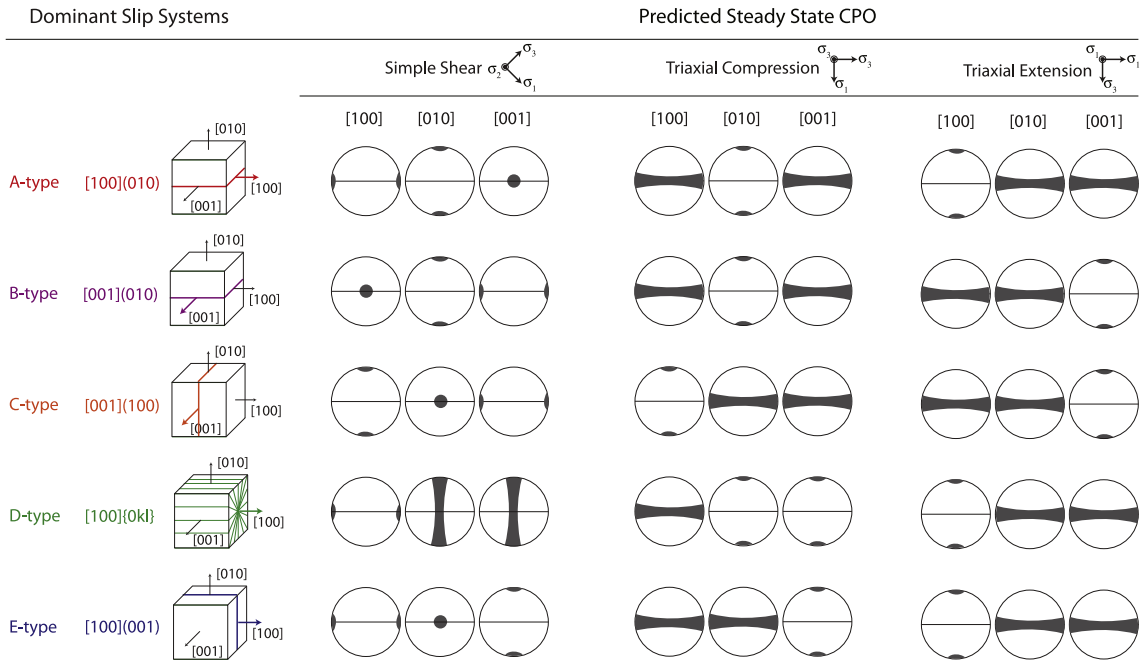

Fig. 4. Diagram illustrating the spectrum of olivine CPOs expected to form for a range of stress states and slip-system activities. Slip directions (i.e. the Burgers vector for the dominant slip system) are assumed to align with the direction of maximum extension, and the slip planes are assumed to align perpendicularly to the direction of maximum shortening. In these simplified pole figures, only point maxima and girdles are shown and the relative strength of these features is not depicted. A- through E-type CPOs refer the CPOs formed in simple shear when one of five slip systems dominates. The same slip system activity will yield different CPOs when the deformation is not simple shear, which are not properly referred to as "A- to E-type". Pole figures are cartoon illustrations of expected steady state CPOs, with smaller gray circles representing point maxima, and gray bands representing girdles of crystal orientations.

specific case of simple shear deformation, which likely dominates plate-driven flow in the asthenosphere (Hager and O'Connell, 1979), the crystallographic slip direction rotates towards the shear direction and the crystallographic slip plane rotates towards the shear plane. However there are several factors that modulate the rate of CPO evolution, and textures in nature may be far from steady-state. In this section we define some criteria for determining whether steady-state texture is achieved, and discuss some factors that influence the rate of CPO evolution.

3.2. Criteria for identifying steady state CPO

CPO in steady state is unmodified by progressive deformation. To determine whether steady state is achieved, observations must show that identical CPOs are generated or found over a range of strains. To form the basis for comparison, CPO may be characterized using a number of tools and quantities. Most commonly, CPO is represented by pole figures, which show in stereographic projection the alignment of grains with respect to some external reference frame. More generally, CPO may be represented by an orientation distribution function (ODF), which describes the distribution of grain orientations as defined by a set of Euler-angle rotations (e.g. Bunge, 1982). In the Earth sciences graphical representations of CPO, such as pole figures, are preferred for the ease with which they can be interpreted. Qualitative descriptions of pole figures are widely used to assess similarities or differences between CPO. However for robust comparison of CPOs, quantitative measures are desirable.

A common quantity associated with CPO is its "strength" or the degree to which grains are aligned in the aggregate. Rocks with weak CPOs have grains with orientations that are distributed in a nearly uniform manner. Rocks with strong CPOs have grains that are highly aligned. There are several widely used metrics for describing CPO strength, but all exhibit a simple monotonic relationship with the magnitude of seismic anisotropy (Mainprice et al., 2014). Other quantities may be used to describe the symmetry of texture. For example, an eigenvalue approach described by (Vollmer, 1990) can be used to assess the degree to which pole figures are characterized by point maxima, by radially symmetric girdles, or by uniform distributions of crystallographic orientations (e.g. Boneh and Skemer, 2014; Higgie and Tommasi, 2012; Soustelle et al., 2010). Finally, simple quantitative measures can also be used to describe the orientation of CPO, for example the angle between a cluster of grains and a kinematic reference frame (Kaminski and Ribe, 2001; Skemer et al., 2012; Warren et al., 2008; Zhang and Karato, 1995). For CPO to be described as steady state, we assert that each of these quantities – strength, symmetry, and orientation of CPO – must also be in steady state.

3.3. Texture evolution due to changes in deformation kinematics

In deformed rocks, CPO develops mainly through the incremental accumulation of strain. In the simple case where strain accumulates linearly and each strain increment is identical, CPO development is relatively straightforward. For example, in the study by Zhang and Karato (1995), the starting material was hot-pressed, isotropic, polycrystalline olivine, and experiments to various strains were performed using a constant deformation geometry and strain-rate. Under these conditions, olivine CPO is observed to strengthen and rotate with progressive strain in a predictable way, and becomes aligned with the shear direction at relatively small shear strains (Fig. 3). Numerical models such as D-REX, when calibrated to the Zhang and Karato (1995) results, also develop strong, well aligned CPOs at relatively small strains (Kaminski and Ribe, 2001). However there are many scenarios in nature where strain histories are complex, and CPO is correspondingly affected. When changes in CPO lag significantly behind changes in kinematics, interpretation of seismic anisotropy must be modified accordingly (Boneh and Skemer, 2014; Boneh et al., 2015; Kaminski and Ribe, 2002; Lassak et al., 2006; Li et al., 2014; Skemer et al., 2012).

Shear zones that intersect larger bodies of previously deformed rock provide an opportunity to assess two sequential stages of deformation, effectively serving as a large-scale rock deformation experiment. Studies in the Josephine Peridotite (Southeastern Oregon, United States)

(Hansen and Warren, 2015; Skemer et al., 2010; Warren et al., 2008) and in the Red Hills (New Zealand) (Webber et al., 2010) suggest that the re-orientation of CPO in rocks with pre-existing texture requires larger strains than one would expect based on the observations by Zhang and Karato (1995) and other experimental studies (Bystricky et al., 2000). In Warren et al. (2008) and Hansen and Warren (2015) the authors describe a 40 m wide zone of localized deformation that intersects at a high angle a larger ophiolite tectonite. The pre-existing fabric in the Josephine peridotite has a foliation that is sub-horizontal while the shear zone is nearly vertical. Deflection of the original compositional foliation by the shear zone provides a precise record of the strain magnitude during the second stage of deformation. Rocks from across this shear zone exhibit a range of deformation histories. Each sample is assumed to have experienced the same first stage of deformation, but the magnitude of shear strain imposed by the second stage of deformation varies with position across the shear zone. When the second stage of deformation is relatively small (i.e. near the margins of the shear zone), CPOs are minimally altered from the first stage of deformation. These samples still exhibit a strong texture, albeit one that is oriented at a high angle to the kinematics of deformation. At moderate strains ($\gamma = 2$–4) olivine [100] axes have rotated, but are still oriented at a high angle to the shear direction, indicating that the CPO has not reached the presumed steady state (Fig. 3). Samples that have experienced the largest strains during the second stage of deformation ($\gamma > 4$) have a CPO that is aligned in a sensible way with the shear zone kinematics. The strength of the CPOs is found to be highly variable, and exhibits no obvious trend as a function of strain. Symmetry also continues to evolve as a function of shear strain. (Hansen and Warren, 2015). Based on these observations, and comparisons with experimental data, the authors conclude that CPO evolution is protracted, and likely influenced by the pre-existing texture.

Recent experiments by Boneh and Skemer (2014) investigate directly the effect of deformation history on olivine CPO evolution. In this study, the starting material used is Åheim dunite, which has a moderately strong pre-existing texture. Experiments were conducted at high temperature and pressure (1200 °C, 1 GPa) in a triaxial geometry (Fig. 2a). Samples were deformed in three configurations, in which shortening was imposed perpendicularly, obliquely, and parallel to the pre-existing foliation. These three experimental configurations allowed the authors to simulate three different deformation histories. CPO was characterized by pole figures, and their strength, symmetry, and orientation. Although the maximum strains achieved in the triaxial geometry are relatively small ($\varepsilon \sim 0.7$), the results reinforce observations from nature. In none of the sample configurations was CPO observed to reach steady state. Moreover, the evolution of CPO in each of the three configurations was distinct. Samples in the perpendicular configuration developed axially symmetric texture, consistent with theoretical predictions (Ribe and Yu, 1991; Wenk et al., 1991) and previous experimental studies (Nicolas et al., 1973). Samples deformed in the oblique and parallel configurations developed more complex CPOs, reflecting the both the partial inheritance of the pre-existing CPO, and the difficulty of "resetting" CPO.

Subsequent numerical simulations by Boneh et al. (2015), using D-Rex and VPSC models, have identified many trends that reinforce the experimental and geologic observations described above. Models that are initiated with a pre-existing texture require greater strain (in many cases 3–5 times the strain magnitude) to approach steady-state than models initiated with a uniform texture. Moreover, models initiated with pre-existing texture exhibit a wide spectrum of behavior, depending on the specific orientation of the pre-existing texture (e.g. Fig. 3). Comparison between models and experiments suggest that models are broadly successful at reproducing the symmetry and the orientation of the experimental CPO. However there are some notable exceptions described in Boneh et al. (2015), in which models predict CPO with anisotropy that is perpendicular to the comparable experimental observation. In comparison to experimental and geologic observations, models tend to evolve quickly and generate CPOs that are relatively strong at low strains. This is particularly true when the models are parameterized through comparison with experiments initiated with uniform textures (i.e. Zhang and Karato, 1995). To some extent, rapid evolution and overly strong textures can be suppressed by modifying the parameters used in the models (see Boneh et al., 2015 for details) or by introducing new schemes for simulating dynamic recrystallization (Signorelli and Tommasi, 2015).

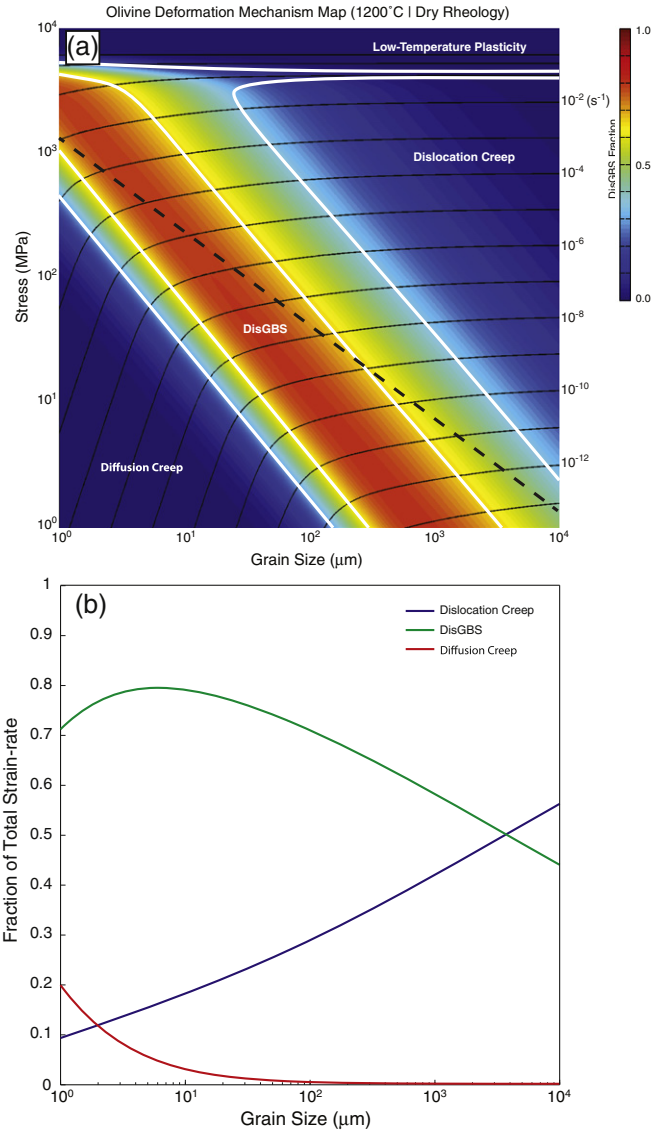

Fig. 5. (a) A deformation mechanism map for olivine calculated using flow laws for dislocation creep and diffusion creep (Hirth and Kohlstedt, 2003), dislocation accommodated grain boundary sliding (disGBS) (Hansen et al., 2011), and low temperature plasticity (Mei et al., 2010). Flow laws are calculated at a temperature of 1200 °C assuming a "dry" rheology. Black lines are contours of constant strain-rate. White lines bound regions where greater than 65% of the total strain rate is accommodated by a single deformation mechanism. Between these domains there is a significant contribution (i.e. >35%) from secondary deformation mechanisms. Colors show the relative fraction of deformation accommodated by the disGBS mechanism ($\dot{\varepsilon}_{disGBS} / \dot{\varepsilon}_{total}$). The dashed black line shows the piezometric relationship between steady-state recrystallized grain size and flow stress for olivine (Van der Wal et al., 1993). (b) The fraction of total strain-rate for each deformation mechanism calculated at each point along the grain-size piezometer. The maximum contribution from the disGBS mechanism is 79%, at a grain-size of ~5 μm. There are no conditions under which a single deformation mechanism contributes more than 80% to the total strain-rate, complicating the interpretation of CPO evolution in nature and in laboratory experiments.

3.4. Texture evolution due to changes in deformation mechanism activity

As with changes in deformation kinematics, changes in the relative activity of different deformation mechanism may initiate long transient intervals in which CPO evolves towards a new steady state.

Crystalline materials at high temperature may deform by several distinct mechanisms. The relative importance of these mechanisms depends on the grain-size and the deformation conditions. The range of conditions that favor a particular deformation mechanism are illustrated using a deformation mechanism map, which is calculated using empirically derived flow laws for each mechanism (Frost and Ashby, 1982). Each deformation mechanism influences CPO evolution differently. Hence, a change in deformation mechanism may lead to evolution of texture towards a new steady state.

At high temperature, high stresses, and large grain-sizes, olivine deformation is accommodated mainly by dislocation creep (Fig. 5a). Due to the inherent asymmetry caused by limited slip systems, dislocation creep generates strong CPOs with predictable relationships between the slip systems and the deformation geometry (Karato et al., 2008). When grain-size or stress is reduced, olivine undergoes a rheological transition, with deformation proceeding by dislocation accommodated grain-boundary sliding (disGBS). Deformation by disGBS involves the relative motion of grain-boundaries; irregularities in the grain boundary are relaxed through the motion of lattice dislocations. Most laboratory experiments are conducted under conditions where disGBS contributes significantly to deformation, and these experiments indicate that disGBS generates CPO in a similar way to dislocation creep (Hansen et al., 2011, 2012). Further reduction in grain-size and/or stress yields a second transition from disGBS to diffusion creep. During diffusion creep, grain-boundary sliding is also presumed to be important, however the accommodating mechanism is primarily diffusion and grain-boundary migration. Without the asymmetry imposed by dislocation motion, it is generally assumed that during diffusion creep no CPO is generated, and pre-existing CPO should be progressively obliterated. Indeed, many fine-grained and highly deformed mylonites exhibit random or progressively weakening CPOs (e.g. Skemer and Karato, 2008; Wallis et al., 2011; Warren and Hirth, 2006). However the influence of diffusion creep on CPO is still far from clear. Theory and observation each suggest that the randomization of CPO by diffusion creep may be quite inefficient and that pre-existing CPOs may be readily preserved at shear strains in excess of $\gamma = 2$ (Wheeler, 2009). Some experiments have also shown the strengthening of olivine CPO during Newtonian creep, although in all cases a secondary phase is involved in texture development (Miyazaki et al., 2013; Sundberg and Cooper, 2008).

One challenge for the interpretation of the relationship between texture and deformation mechanism is that several mechanisms may be operating simultaneously. To illustrate this point we return to the deformation mechanism map for olivine (Fig. 5a). On this map is included the empirically calibrated grain-size piezometer for olivine from Van der Wal et al. (1993). This line shows the expected relationship between steady-state grain-size and flow stress in a deforming, unannealed rock. We can examine the locus of points along this piezometer and ask what fraction of each deformation mechanism contributes to the total strain (rate) (Fig. 5b). At 1200 °C, the maximum contribution from disGBS occurs at a grain-size of 5 μm, corresponding to a flow stress of ~400 MPa. At these conditions, disGBS contributes 79% of the total strain-rate, while dislocation creep and diffusion creep each contribute substantively to the remaining fraction (16% and 5%, respectively). At lower stress conditions, diffusion creep becomes less important, however dislocation creep and disGBS may contribute sub-equally to the total deformation rate. At no point along the trend of the grain-size piezometer does one deformation mechanism contribute more than 80% of the total strain (-rate).

Since each deformation mechanism modifies CPO in different ways, it is important to consider how CPO accumulates when multiple mechanisms are operative. Although there are little experimental data available, there is at least some indication that CPO evolution is slowed when diffusion creep and disGBS are suppressed. For example, Skemer et al. (2011) performed torsion experiments on coarse-grained dunite under conditions where dislocation creep was strongly favored. Examining the microstructural evolution in the unrecrystallized fraction the authors conclude that CPO evolution, specifically the rotation towards the shear plane, requires significantly larger strain than in the comparable experiments by Zhang and Karato (1995) (Fig. 3). However in this type of study it is difficult to decouple the effects of grain-size and deformation mechanism, dynamic recrystallization, and pre-existing texture. Experiments by Hansen et al. (2014, see their Fig. 6b) do exhibit a subtle decrease in CPO strength with decreasing grain size, potentially indicating the increased influence of grain-size sensitive deformation mechanisms at fine grain-sizes. We speculate that even small (~10% of the total strain-rate) contributions from secondary deformation mechanisms may contribute in a measureable way to the evolution of CPO. However, the exact threshold is unknown, and there is a clear need for further detailed investigations of the role of combined deformation mechanisms on texture evolution.

3.5. Texture evolution due to changes in thermodynamic state

As noted in previous sections, CPO evolution is strongly influenced by the thermodynamic state, including the temperature and pressure of deformation, and the concentration of small amounts of water. As the mantle convects materials are advected through a wide range of deformation conditions. For example, in the mantle wedge of a subduction zone, temperature, pressure, and water concentration may all change incrementally as the slab entrains mantle wedge material downward through the zone where the oceanic crust dehydrates (e.g. Cagnioncle et al., 2007). If the strains required for CPO reorganization are large in comparison to the strain induced between each substantial change in the deformation conditions, the CPO will reflect the complexities of the deformation history (Lassak et al., 2006). As such, interpretations of seismic anisotropy in subduction settings must consider both the complexities introduced by evolving deformation conditions, in addition to changes in the deformation kinematics.

4. The interpretation of seismic anisotropy

The rich detail now documented in the development of olivine textures suggests that information may be available beyond that typically sought in seismological studies. For instance, traditional estimates of flow in the upper mantle from seismic anisotropy only estimate shear direction without indicating the sense of shear (Hess, 1964; Tanimoto and Anderson, 1984). However, it is possible that spatial variations in the orientation of anisotropy can indicate the shear sense, and therefore the sign of the velocity gradient (Skemer et al., 2012). The scope of the information that can be retrieved depends on the degree to which details of the textural evolution can be resolved in observations of seismic anisotropy. Important aspects of relating texture to seismic observables include determining the relevant measures of anisotropy for a specific application, the micromechanical aspects of relating single-crystal properties to aggregate properties, and the link between texture and kinematics.

4.1. Calculating seismic anisotropy from texture

Forward modeling of seismic anisotropy requires conversion from a quantification of the microstructural state to elastic tensors for a representative volume element. This procedure is complicated by the non-trivial interactions of anisotropic grains in a polycrystalline aggregate and the spatial distribution and interconnectivity of secondary phases.

Assuming a sufficient number of grains have been sampled, individual measurements of grain orientations provide a first order estimate of the elastic properties of the aggregate. The elastic tensor of each grain is

rotated into the sample reference frame, and the rotated tensors of all the grains are averaged according to a preferred effective-medium theory. Effective-medium theories for linear elasticity are bound by two end members, assuming either the elastic strain (Voigt bound) or the stress (Reuss bound) is homogeneous throughout the aggregate. These two bounds correspond to taking either the arithmetic mean or harmonic mean of the stiffnesses, respectively. Often these two bounds are then averaged arithmetically. (i.e. Hill, 1952), referred to now as the Hill average.

Such methods have been used for several decades to successfully predict anisotropy and velocity in ultrasonic laboratory tests, employing texture measurements made with a universal-stage microscope (Babuška, 1972; Baker and Carter, 1972; Crosson and Lin, 1971; Fountain, 1976; Klíma and Babuška, 1968). Notably, some ultrasonic studies of textured peridotites indicate that the aggregate anisotropy is best approximated using the Voigt bound (Crosson and Lin, 1971; Peselnick et al., 1974). A similar conclusion has been drawn for plagioclase rich rocks (Seront et al., 1993). However, because the CPOs in the samples measured in these ultrasonic studies tended to be of a single type, it remains unclear if the Voigt bound is the best predictor of the magnitude of anisotropy for all CPO types of interest.

The introduction of EBSD to the Earth sciences (Prior et al., 1999) has greatly simplified texture measurement and, therefore, calculation of seismic characteristics of textured rocks. ODFs can be quickly calculated from EBSD data, and the calculation of elasticity tensors from those ODFs easily automated, for instance with MATLAB toolboxes such as MTEX (Mainprice et al., 2011) or MSAT (Walker and Wookey, 2012). Elastic properties calculated using EBSD data and Voigt, Reuss, or Hill averaging schemes are comparable to those measured with ultrasonic techniques in both metals and rocks. Comparison between EBSD data and ultrasonic tests in aluminum (Davis et al., 2008) and steel (Niehuesbernd et al., 2013) indicates EBSD sufficiently captures the inherent elastic properties as long as a large enough area is mapped to characterize heterogeneity in the microstructure. However, secondary features like fractures significantly influence the ultrasonic measurement but are not captured by EBSD. In a more sophisticated approach, Zhong et al. (2014) compared ultrasonic measurements to elastic properties calculated using a finite-element method with purely elastic rheology. EBSD data was used to explicitly define the microstructure in the finite-element discretization, including serpentine-filled fractures. The authors found significantly improved agreement with ultrasonic measurement compared to traditional averaging schemes, importantly noting that the fractures contributed to some of the anisotropy measured in the ultrasonic tests. In addition, although the Voigt average may be the best predictor of the magnitude of anisotropy, Zhong et al. (2014) found that the magnitudes of individual elastic constants are best approximated by the Hill average.

The presence of secondary phases in a rock further complicates the calculation of elastic properties. If the phases are evenly distributed throughout the rock such that the phase distribution is isotropic, a reasonable estimate of the rock properties can be obtained by first calculating the aggregate elastic tensors for each phase based on the ODF for grains of that phase, and subsequently taking the weighted arithmetically averaged of those tensors with a weight proportional to the volume fraction of each phase. This technique has been applied to both crustal rocks (e.g. Cao et al., 2014; Erdman et al., 2013; Tatham et al., 2008) and mantle rocks (e.g. Ben Ismail et al., 2001; Mainprice and Silver, 1993). Notably, Tatham et al. (2008) applied this technique to lower-crustal rocks and demonstrated its usefulness in assessing the variation in seismic characteristics over a continuous range of rock types. This numerical modification of the secondary phase content has proved useful in laboratory-based studies in which, for example, samples are almost entirely olivine, but the seismic characteristics of olivine–pyroxene mixtures are desired (e.g. Hansen et al., 2014).

If the phase distribution is not isotropic, further steps must be taken to calculate aggregate properties. If the material is made up of compositionally distinct layers in which the layers are isotropic, the layering induces hexagonal anisotropy (transverse isotropy) that can be estimated with the Backus average (Backus, 1962). If the individual layers are themselves anisotropic, more sophisticated schemes are available for averaging elasticity tensors assuming fine-scale layering (Schoenberg and Muir, 1989). If the microstructure is more complicated than homogeneous layering, a technique that explicitly accounts for the observed microstructure will be necessary, such as approaches based on the finite-element method of Zhong et al. (2014).

4.2. Standard measures of seismic anisotropy

Given that elastic moduli are commonly described by fourth-rank tensors made up of 81 coefficients, 21 of which are independent, it is not surprising that a variety of methods exist for describing the magnitude and orientation of elastic anisotropy. A comprehensive review of terminology for elastically anisotropic minerals is given by Mainprice (2015). Here we touch on a few of the most popular metrics.

Given a full stiffness or compliance tensor, it is straightforward to calculate the velocity of a P-wave and of the two polarized S-waves for any propagation direction using the Christoffel equation, (e.g. Schulte-Pelkum and Blackman, 2003). As shown in Fig. 1 these velocities can be plotted on a stereonet in the crystallographic or geographic reference frame to visualize the details of anisotropy. Furthermore, the polarization directions of S-waves can be projected onto the plane of the stereonet, yielding a convenient method for predicting seismic observables such as the direction of shear-wave splitting (e.g. Holtzman and Kendall, 2010; Song and Kawakatsu, 2012).

In addition to this visualization, the magnitude of P-wave anisotropy can be defined as a scalar by

$$dV_{\mathrm{p}} = \frac{V_{\mathrm{p,\,max}} - V_{\mathrm{p,\,min}}}{V_{\mathrm{p,\,avg}}} \tag{1}$$

and the magnitude of S-wave anisotropy for the two polarizations can be defined as

$$dV_{\mathrm{S1}} = \frac{V_{\mathrm{S1,\,max}} - V_{\mathrm{S1,\,min}}}{V_{\mathrm{S1,\,avg}}} \tag{2}$$

and

$$dV_{\mathrm{S2}} = \frac{V_{\mathrm{S2,\,max}} - V_{\mathrm{S2,\,min}}}{V_{\mathrm{S2,\,avg}}} \tag{3}$$

where the V_{P}, V_{S1}, and V_{S2} are the velocities of the P-wave and two polarizations of the S-wave, respectively. The subscripts min, max, and avg indicate the minimum values, maximum values, and average values, respectively. These metrics are often less convenient for comparison to seismological models, which rarely include the full 3-dimensional dependence of P- and S-wave velocity on propagation direction. Often, anisotropic inversions of seismic data are cast in terms of the Love parameters, A, C, F, L and N (Anderson and Dziewonski, 1982; Love, 1927; Montagner and Nataf, 1986; Takeuchi and Saito, 1972). These parameters are related to the coefficients of the stiffness tensor, C, by (in Voigt notation)

$$\begin{aligned} A &= C_{11} \\ C &= C_{33} \\ F &= C_{13} \\ L &= C_{44} = C_{55} \\ N &= C_{66} = \frac{1}{2}(C_{11} - C_{12}). \end{aligned} \tag{4}$$

This formulation assumes that the medium is transversely isotropic (i.e., hexagonal symmetry) with a vertical symmetry axis (corresponding to the 3 axis). As noted above, olivine CPOs with transverse isotropy

tend to form in compression tests, but CPOs formed in simple shear tend to have orthorhombic symmetry. In the special case of transverse isotropy, one S-wave will be polarized in the horizontal plane and the other will be polarized in the vertical plane. Thus, a common measure of anisotropy utilizing the Love parameters is the radial anisotropy,

$$\xi = \left(\frac{V_{SH}}{V_{SV}}\right)^2 = \frac{N}{L}, \tag{5}$$

which, to a first order, can be used to characterize the discrepancy between Love waves and Raleigh waves. Montagner and Nataf (1986) expanded the Love parameters to account for general anisotropy,

$$\begin{aligned} A &= \frac{3}{8}(C_{11}+C_{22})+\frac{1}{4}C_{12}+\frac{1}{2}C_{66} \\ C &= C_{33} \\ F &= \frac{1}{2}(C_{13}+C_{23}) \\ L &= \frac{1}{2}(C_{44}+C_{55}) \\ N &= \frac{1}{8}(C_{11}+C_{12})-\frac{1}{4}C_{12}+\frac{1}{2}C_{66}. \end{aligned} \tag{6}$$

Furthermore, they introduced 8 additional terms that depend on the azimuth of the incident wave. The magnitude of azimuthal anisotropy is given by

$$\begin{aligned} G_c &= \frac{1}{2}(C_{55}-C_{44}) \\ G_s &= C_{54}. \end{aligned} \tag{7}$$

Clearly, inversions of seismic data that assume transverse isotropy should be interpreted with care (Becker et al., 2006), considering that the true anisotropy likely has lower degrees of symmetry, as evidenced by observations of CPOs in both naturally and experimentally deformed rocks (Ben Ismail and Mainprice, 1998; Christensen and Lundquist, 1982; Karato et al., 2008; Mainprice, 2015; Mercier and Nicolas, 1975; Nicolas and Christensen, 1987; Nicolas et al., 1971). For instance, if a region in Earth were sampled by ray paths with a wide range of azimuths, a value for ξ calculated assuming transverse isotropy should be reasonably approximated by N/L in the latter set of equations. However, if the azimuthal coverage is poor, values of ξ will depend on the dominant azimuth sampled. Additional methods are available in which the stiffness tensor can be decomposed into components with different symmetries (Browaeys and Chevrot, 2004). In this manner, one can evaluate the degree to which non-hexagonal components of the tensor contribute to the anisotropy, and therefore assess the validity of assuming transverse isotropy.

The symmetry of the texture developed during deformation may also lead to observable differences in seismic anisotropy. As described above, it is well documented that compressional deformation of dry olivine aggregates tends to produce textures that are transversely isotropic. Additionally, numerical simulations (Knoll et al., 2009) and recent experiments (Hansen et al., in prep), demonstrate that extensional deformation also tends to produce transversely isotropic textures (e.g. Fig. 4). However, axial compression yields values of $\xi > 1$ while axial tension case yields values of $\xi < 1$, assuming the loading axis is vertical. Additional complications arise when deformation is predominantly simple shear, as most simple-shear deformation yields monoclinic or orthorhombic textures. Although the strength of CPO and the consequent magnitude of ξ appears to saturate at large deformations in simple shear (Fig. 6), ξ will also depend on the orientation of the shear plane. For typical olivine A-type CPOs, vertical shear yields values of $\xi < 1$ and horizontal shear yields values of $\xi > 1$. Different olivine CPO types will yield different relationships between shear direction and ξ (Karato et al., 2008).

The magnitude and direction of shear wave splitting is another metric commonly derived from seismic data. The direction of the fast shear wave in a homogenous medium is determined from the elasticity

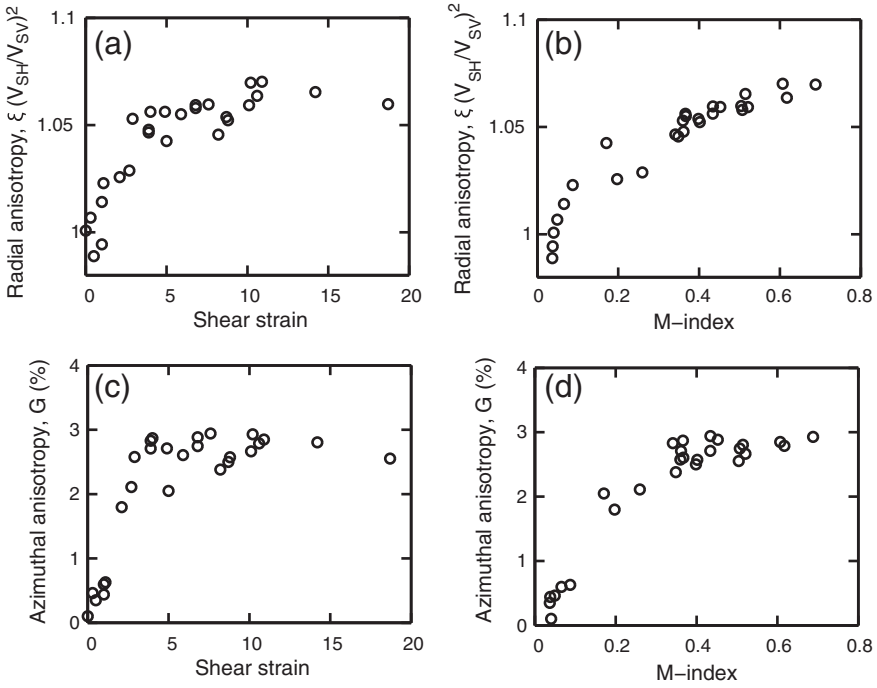

Fig. 6. Magnitude of seismic anisotropy as a function of strain (a, c) and texture strength (b, d) in laboratory-based deformation experiments (Hansen et al., 2014). Seismic anisotropy is characterized by the magnitude of radial anisotropy, ξ, and the magnitude of azimuthal anisotropy, *G*. These values were calculated taking the shear plane to be horizontal and using Eqs. (5)–(7). Texture strength is quantified using the M-index, which is scaled from zero (uniform distribution of crystal axes) to one (single crystal texture) (Skemer et al., 2005). Seismic characteristics are calculated from measured olivine textures assuming 40% of the sample volume is orthopyroxene with uniform texture. Although texture strength appears to increase continuously with strain, the magnitude of seismic anisotropy saturates at shear strains of $\gamma = 5$–10.

tensor. The Christoffel tensor, T, can be determined from the stiffness tensor and the propagation direction of the wave of interest, n, (Love, 1927, pp. 298–299),

$$T_{ik} = C_{ijkl} n_j n_i. \quad (8)$$

The eigenvectors of T_{ik} correspond to the polarization directions of the P-wave, the fast S-wave, and the slow S-wave, in order of decreasing eigenvalue. Determination of the delay time between the two shear waves depends on the distance traveled in the medium, but calculation of this value becomes convoluted once the elastic parameters vary along the ray path. Simple averaging schemes are possible for forward modeling delay times (Bonnin et al., 2012; Montagner et al., 2000), but full-waveform methods (Chevrot, 2006; Chevrot et al., 2004; Komatitsch and Tromp, 1999) are likely the most robust approach, allowing the dependence of back azimuth to be taken into account (Becker et al., 2012). That said, full-waveform methods are computationally expensive and are largely in agreement with the simpler averaging methods when smooth tomographic models are implemented (Becker et al., 2012).

4.3. Time-scales for the development of seismic anisotropy

As discussed in Section 3, the formation of CPO is not instantaneous but instead evolves over an increment of time (or strain). It follows, therefore, that the formation of seismic anisotropy is also time (or strain) dependent. Fig. 6 presents one example of the dependence of anisotropy on both shear strain and texture strength, which was measured in torsion experiments on olivine aggregates (Hansen et al., 2014). In these experiments texture strength is found to increase with strain but also appears to reach a saturation point at shear strains greater than ~10. This saturation point corresponds to a fabric strength of approximately M = 0.4, a relatively high value for a natural sample. Fig. 6 illustrates the dependence of the calculated seismic anisotropy on the measured texture, which, as initially pointed out by Ben Ismail and Mainprice (1998), exhibits a clear non-linear relationship. As texture strength becomes increasingly strong, the corresponding increase in anisotropy diminishes. Fig. 6 also shows that the magnitude of anisotropy reaches an apparent steady state at shear strains of ~5, faster than the texture strength appears to reach a steady state. This may reflect, in part, the challenge of using a single scalar measure to quantify CPO strength.

The evolution of seismic anisotropy will also depend on the strain path. If the kinematics of the deformation evolve, so will the texture. As the evolution of texture may lag significantly behind the kinematics, care must be taken in assessing flow direction from seismic anisotropy. As mentioned in Section 3.3, Boneh and Skemer (2014) and Hansen et al. (in prep) have documented the protracted evolution of anisotropy after marked changes in the kinematics are imposed in a laboratory experiment. These observations has been corroborated by numerical simulations (Boneh et al., 2015). The timescale over which the magnitude and symmetry of anisotropy evolves is influenced significantly by the specific details of the deformation history. In the experiments by Hansen et al., (in prep) anisotropy is similar in samples deformed with complex kinematics (tension followed by torsion) and those deformed simply in torsion. However the orientation of anisotropy in samples initially deformed in tension does lag slightly behind those deformed solely in torsion. Collectively, these data suggest that most of the development of seismic anisotropy will occur once shear strains of ~5 are reached regardless of the kinematic history, although there may be outliers for specific scenarios (Boneh and Skemer, 2014). The largest variation, in all cases, is observed at smaller strains. Thus, the magnitude and the orientation of anisotropy may be an important indicator of strain rates in regions with strong gradients in the magnitude of strain (e.g., new transform faults, rift systems) or in the geometry of deformation (e.g., corner flow near mid-Ocean ridges, flow around slab edges at subduction zones).

4.4. Implications for interpreting seismological data sets

This discussion highlights two important predictions regarding upper-mantle seismic anisotropy that are revealed by laboratory experiments. First, the symmetry of anisotropy depends on the geometry of deformation and the integrated strain history, parameters that are rarely accounted for in interpretations of seismological data sets. Second, the strength, symmetry, and orientation of anisotropy should not be assumed to quickly reach a steady state, especially for deformation paths with changing kinematics.

Assumptions of certain symmetries are common in seismic studies. The Preliminary Reference Earth Model explicitly assumes transverse isotropy of the upper mantle (Dziewonski and Anderson, 1981), as do many global seismic inversions (Ekstrom and Dziewonski, 1998; Nettles and Dziewoński, 2008; Panning and Romanowicz, 2006; Shapiro and Ritzwoller, 2002). The upper mantle, however, does exhibit significant azimuthal anisotropy. This is especially true in the vicinity of ocean plates, where deformation kinematics are often dominated by directionally consistent shear of the underlying asthenosphere (e.g. Montagner and Tanimoto, 1991). As much of the upper mantle exhibits azimuthal anisotropy, inversions that assume transverse isotropy will introduce a dependence on path coverage particularly over large regions such as the Pacific that represent a large fraction of upper mantle anisotropy (Auer et al., 2014; Ekström, 2011; Laske and Masters, 1998). The choice to neglect azimuthal anisotropy is often necessary given the limited number of parameters that can be constrained by seismological data. Nonetheless, future efforts will continue to benefit from considering the implications of assuming transverse isotropy.

Shear-wave splitting measurements are also affected significantly by the symmetry of anisotropy. For example, several studies have noted that when the fastest wave-propagation direction is dipping, various symmetries of anisotropy can result in splitting directions that differ by up to 90° (Chevrot and van der Hilst, 2003; Skemer et al., 2012; Song and Kawakatsu, 2012). Abt and Fischer (2008), following a similar line of thinking, used shear wave splitting tomography to explore the three-dimensional distribution of shear wave splitting anisotropy, given various assumptions about hexagonal or orthorhombic symmetry and dipping interfaces (Abt et al., 2009). Due to the significant component of vertical flow expected near plate boundaries, regional studies should be strongly affected by assumptions about the symmetry and orientation of the anisotropy (Becker et al., 2006). Although availability and density of seismological data fundamentally limit our ability to resolve general anisotropy, there is an opportunity for future studies to look specifically for spatial variations in the symmetry of anisotropy, which can be linked to variations in deformation geometry or the magnitude of deformation in a physically meaningful way.

The evolution of CPO is now recognized to be a protracted process that yields long transient intervals in which steady-state CPO and seismic anisotropy are not reached. Becker et al. (2014) demonstrated that, in a global sense, observed azimuthal anisotropy in the asthenosphere does not correlate well with the local direction of absolute plate motion, but it does correlate well with azimuthal anisotropy from a convection simulation coupled with a CPO evolution model. Thus, it is natural to conclude that the transient nature of CPO captured by the CPO evolution model is critical in predicting anisotropy. However, even when a CPO evolution model such as D-Rex is used, Becker et al. (2014) still find a poor correlation between flow models and observed anisotropy near plate boundaries where changes in kinematics occur over short spatial/temporal scales. This may reflect the fact that widely-used models such as D-REX do not properly capture the transient evolution of olivine CPO, especially when an initial texture is present (Boneh et al., 2015). It may also reflect in part other complexities including intraplate deformation and along-strike mantle flow. There is, however, an opportunity to exploit the transient evolution of olivine CPO to assess rheological phenomena. For instance, Zietlow et al. (2014) used the spatial variation in the azimuth of shear wave

splitting near the Alpine Fault in New Zealand to constrain gradients in strain rate and therefore make estimates of the rheological behavior of the upper mantle in that region. The obliquity that is preserved in the shear wave splitting data with respect to the geodetically constrained plate motion is consistent with the olivine A-type fabric, suggesting that water contents in the sub-lithospheric mantle may be relatively low (Skemer et al., 2012). Because the symmetry, orientation, and strength of seismic anisotropy all vary as a function of strain, future seismological studies may be able to use heterogeneity in all of these parameters as proxies for the spatial distribution of deformation.

5. Summary and future challenges

Rock deformation experiments and natural observations of olivine CPO provide the conceptual framework for interpreting seismic anisotropy to determine mantle flow and for generating forward models of anisotropy from numerical models of mantle flow. Over the last fifteen years there have been major advances in the study of olivine CPO evolution and its relationship to seismic anisotropy. Nonetheless, interpreting seismic anisotropy in terms of mantle flow is still a non-unique problem and any individual measurement of seismic anisotropy can be interpreted in many ways. A significant challenge is that texture and any associated anisotropy accumulates slowly, and is strongly influenced by changes in deformation mechanisms, kinematics of deformation, or the thermodynamic state. This expands the spectrum of CPOs that may be found under given deformation conditions.

Agreement between forward models and observations in the centers of ocean plates suggests that the broader framework for interpreting seismic anisotropy is robust in cases where deformation is fairly simple. However the poor agreement between models and observations over shorter length scales and especially near plate boundaries implies a need for further exploration, both of the microphysics of rock deformation, and seismological methods.

Looking forward, advances are sought in new experimental data, advanced theoretical predictions of CPO evolution, and higher resolution seismological datasets. On the experimental side, efforts are needed to better understand the time-scales of transient texture evolution; these data are necessary to improve the parameterization of forward models of texture evolution. On the seismological side, further efforts are needed to improve the resolution of anisotropy methods to seek structure at a finer scale and to identify features of anisotropy that can be uniquely interpreted through the framework of experiments and theory. Further use of back-azimuth data to identify dipping (Chevrot and van der Hilst, 2003) or layered structures (Silver and Savage, 1994), use of 3D approaches (Abt and Fischer, 2008), and additional observation close to plate boundaries will be critical. Finally we encourage the complimentary use of forward and inverse modeling approaches to provide the greatest insight into the nature of mantle flow near plate boundaries.

Acknowledgments

The research is supported by NSF EAR-1141795 (to PS) and award 123/718 from the John Fell Oxford University Press Fund (to LH). The authors gratefully acknowledge constructive input from Thorsten Becker and an anonymous reviewer, and thank the editors of Tectonophysics for extending the invitation to write this review.

References

Abt, D.L., Fischer, K.M., 2008. Resolving three-dimensional anisotropic structure with shear wave splitting tomography. Geophys. J. Int. 173, 859–886.
Abt, D.L., Fischer, K.M., Abers, G.A., Strauch, W., Protti, J.M., González, V., 2009. Shear wave anisotropy beneath Nicaragua and Costa Rica: implications for flow in the mantle wedge. Geochem. Geophys. Geosyst. 10. http://dx.doi.org/10.1029/2009gc002375.
Anderson, D.L., Dziewonski, A.M., 1982. Upper mantle anisotropy: evidence from free oscillations. Geophys. J. Int. 69, 383–404.
Andreatta, C., 1934. Analisi strutturali di rocce metamorfiche. V. Oliviniti. Period. Miner. 5, 237–253.
Auer, L., Boschi, L., Becker, T., Nissen-Meyer, T., Giardini, D., 2014. Savani: a variable resolution whole-mantle model of anisotropic shear velocity variations based on multiple data sets. J. Geophys. Res. Solid Earth 119, 3006–3034.
Ave'Lallemant, H.G., Carter, N.L., 1970. Syntectonic recrystallization of olivine and modes of flow in the upper mantle. Geol. Soc. Am. Bull. 81, 2203–2220.
Babuška, V., 1972. Elasticity and anisotropy of dunite and bronzitite. J. Geophys. Res. 77, 6955–6965.
Backus, G.E., 1962. Long-wave elastic anisotropy produced by horizontal layering. J. Geophys. Res. 67, 4427.
Baker, D.W., Carter, N.L., 1972. Seismic velocity anisotropy calculated for ultramafic minerals and aggregates. Flow and Fracture of Rockspp. 157–166.
Becker, T.W., Kellogg, J.B., Ekstrom, G., O'Connell, R.J., 2003. Comparison of azimuthal seismic anisotropy from surface waves and finite strain from global mantle-circulation models. Geophys. J. Int. 155, 696–714.
Becker, T.W., Chevrot, S., Schulte-Pelkum, V., Blackman, D.K., 2006. Statistical properties of seismic anisotropy predicted by upper mantle geodynamic models. J. Geophys. Res. Solid Earth 111.
Becker, T.W., Kustowski, B., Ekström, G., 2008. Radial seismic anisotropy as a constraint for upper mantle rheology. Earth Planet. Sci. Lett. 267, 213–227.
Becker, T., Lebedev, S., Long, M., 2012. On the relationship between azimuthal anisotropy from shear wave splitting and surface wave tomography. J. Geophys. Res. Solid Earth 1978–2012, 117.
Becker, T.W., Conrad, C.P., Schaeffer, A.J., Lebedev, S., 2014. Origin of azimuthal seismic anisotropy in oceanic plates and mantle. Earth Planet. Sci. Lett. 401, 236–250.
Ben Ismail, W., Mainprice, D., 1998. An olivine fabric database; an overview of upper mantle fabrics and seismic anisotropy. Tectonophysics 296, 145–157.
Ben Ismail, W., Barruol, G., Mainprice, D., 2001. The Kaapvaal craton seismic anisotropy: petrophysical analyses of upper mantle kimberlite nodules. Geophys. Res. Lett. 28, 2497–2500.
Birch, F., 1960. The velocity of compressional waves in rocks to 10 kilobars: 1. J. Geophys. Res. 65, 1083–1102.
Birch, F., 1961. The velocity of compressional waves in rocks to 10 kilobars: 2. J. Geophys. Res. 66, 2199–2224.
Blackman, D.K., Kendall, J.M., 2002. Seismic anisotropy in the upper mantle 2. Predictions for current plate boundary flow models. Geochem. Geophys. Geosyst. 3, 1 of 26–26 of 26. http://dx.doi.org/10.1029/2001gc000247.
Boneh, Y., Skemer, P., 2014. The effect of deformation history on the evolution of olivine CPO. Earth Planet. Sci. Lett. 406, 213–222.
Boneh, Y., Morales, L.F., Kaminski, E., Skemer, P., 2015. Modeling olivine CPO evolution with complex deformation histories: implications for the interpretation of seismic anisotropy in the mantle. Geochem. Geophys. Geosyst. 16. http://dx.doi.org/10.1002/2015GC005964.
Bonnin, M., Tommasi, A., Hassani, R., Chevrot, S., Wookey, J., Barruol, G., 2012. Numerical modelling of the upper-mantle anisotropy beneath a migrating strike-slip plate boundary: the San Andreas Fault system. Geophys. J. Int. 191, 436–458.
Brothers, R., 1959. Flow orientation of olivine. Am. J. Sci. 257, 574–584.
Browaeys, J.T., Chevrot, S., 2004. Decomposition of the elastic tensor and geophysical applications. Geophys. J. Int. 159, 667–678.
Bunge, H., 1982. Texture analysis in materials science: mathematical models. Butterworths, London.
Bystricky, M., Kunze, K., Burlini, L., Burg, J.P., 2000. High shear strain of olivine aggregates; rheological and seismic consequences. Science 290, 1564–1567.
Cagnioncle, A.M., Parmentier, E., Elkins-Tanton, L.T., 2007. Effect of solid flow above a subducting slab on water distribution and melting at convergent plate boundaries. J. Geophys. Res. Solid Earth 112.
Cao, Y., Jung, H., Song, S., 2014. Microstructures and petro-fabrics of lawsonite blueschist in the North Qilian suture zone, NW China: implications for seismic anisotropy of subducting oceanic crust. Tectonophysics 628, 140–157.
Carter, N.L., Ave Lallemant, H.G., 1970. High temperature flow of dunite and peridotite. Geol. Soc. Am. Bull. 81, 2181–2202.
Carter, N.L., Baker, D.W., George, R.P., 1972. Seismic anisotropy, flow, and constitution of the upper mantle. Flow and Fracture of Rockspp. 167–190.
Castelnau, O., Blackman, D.K., Lebensohn, R.A., Ponte Castañeda, P., 2008. Micromechanical modeling of the viscoplastic behavior of olivine. J. Geophys. Res. 113. http://dx.doi.org/10.1029/2007jb005444.
Castelnau, O., Blackman, D.K., Becker, T.W., 2009. Numerical simulations of texture development and associated rheological anisotropy in regions of complex mantle flow. Geophys. Res. Lett. 36. http://dx.doi.org/10.1029/2009gl038027.
Chastel, Y.B., Dawson, P.R., Wenk, H.R., Bennett, K., 1993. Anisotropic convection with implications for the upper-mantle. J. Geophys. Res. Solid Earth 98, 17757–17771.
Chevrot, S., 2006. Finite-frequency vectorial tomography: a new method for high-resolution imaging of upper mantle anisotropy. Geophys. J. Int. 165, 641–657.
Chevrot, S., van der Hilst, R.D., 2003. On the effects of a dipping axis of symmetry on shear wave splitting measurements in a transversely isotropic medium. Geophys. J. Int. 152, 497–505.
Chevrot, S., Favier, N., Komatitsch, D., 2004. Shear wave splitting in three-dimensional anisotropic media. Geophys. J. Int. 159, 711–720.
Christensen, N., Crosson, R., 1968. Seismic anisotropy in the upper mantle. Tectonophysics 6, 93–107.
Christensen, N.I., Lundquist, S.M., 1982. Pyroxene orientation within the upper mantle. Geol. Soc. Am. Bull. 93, 279–288.
Conder, J.A., Wiens, D.A., 2007. Rapid mantle flow beneath the Tonga volcanic arc. Earth Planet. Sci. Lett. 264, 299–307. http://dx.doi.org/10.1016/j.epsl.2007.10.014.

Conrad, C.P., Behn, M.D., 2010. Constraints on lithosphere net rotation and asthenospheric viscosity from global mantle flow models and seismic anisotropy. Geochem. Geophys. Geosyst. 11.

Conrad, C.P., Behn, M.D., Silver, P.G., 2007. Global mantle flow and the development of seismic anisotropy: differences between the oceanic and continental upper mantle. J. Geophys. Res. 112. http://dx.doi.org/10.1029/2006jb004608.

Couvy, H., Frost, D.J., Heidelbach, F., Nyilas, K., Ungar, T., Mackwell, S., Cordier, P., 2004. Shear deformation experiments of forsterite at 11GPa–1400 degrees C in the multianvil apparatus. Eur. J. Mineral. 16, 877–889.

Crosson, R.S., Lin, J.W., 1971. Voigt and Reuss prediction of anisotropic elasticity of dunite. J. Geophys. Res. 76, 570–578.

Davis, C., Strangwood, M., Potter, M., Dixon, S., Morris, P., 2008. Prediction of elastic modulus + anisotropy using x-ray and electron backscattered diffraction texture quantification and ultrasonic (electromagnetic acoustic transducer) measurements in aluminum sheets. Metall. Mater. Trans. A 39, 679–687.

Dziewonski, A.M., Anderson, D.L., 1981. Preliminary reference Earth model. Phys. Earth Planet. Inter. 25, 297–356.

Ekström, G., 2011. A global model of Love and Rayleigh surface wave dispersion and anisotropy, 25–250 s. Geophys. J. Int. 187, 1668–1686.

Ekstrom, G., Dziewonski, A.M., 1998. The unique anisotropy of the Pacific upper mantle. Nature 394, 168–172.

Erdman, M.E., Hacker, B.R., Zandt, G., Seward, G., 2013. Seismic anisotropy of the crust: electron-backscatter diffraction measurements from the Basin and Range. Geophys. J. Int. 195, 1211–1229.

Faccenda, M., Capitanio, F.A., 2012. Development of mantle seismic anisotropy during subduction-induced 3-D flow. Geophys. Res. Lett. 39. http://dx.doi.org/10.1029/2012gl051988.

Fountain, D.M., 1976. The Ivrea—Verbano and Strona–Ceneri Zones, Northern Italy: a cross-section of the continental crust—new evidence from seismic velocities of rock samples. Tectonophysics 33, 145–165.

Frost, H., Ashby, M., 1982. Deformation-mechanism maps: the plasticity and creep of metals and ceramics. 1st edition. Pergamon Press.

Hager, B.H., O'Connell, R.J., 1979. Kinematic models of large-scale flow in the Earth's mantle. J. Geophys. Res. Solid Earth 84 (1978–2012), 1031–1048.

Hansen, L.N., Warren, J.M., 2015. Quantifying the effect of pyroxene on deformation of peridotite in a natural shear zone. J. Geophys. Res. Solid Earth 120, 2717–2738.

Hansen, L.N., Zimmerman, M.E., Kohlstedt, D.L., 2011. Grain boundary sliding in San Carlos olivine: flow law parameters and crystallographic-preferred orientation. J. Geophys. Res. Solid Earth 116.

Hansen, L.N., Zimmerman, M.E., Kohlstedt, D.L., 2012. The influence of microstructure on deformation of olivine in the grain-boundary sliding regime. J. Geophys. Res. Solid Earth 117.

Hansen, L.N., Zhao, Y.-H., Zimmerman, M.E., Kohlstedt, D.L., 2014. Protracted fabric evolution in olivine: Implications for the relationship among strain, crystallographic fabric, and seismic anisotropy. Earth Planet. Sci. Lett. 387, 157–168.

Hansen, L.N., Warren, J.M., Zimmerman, M.E., Kohlstedt, D.L., 2015. Viscous anisotropy of texture olivine aggregates, Part 1: measurement of the magnitude and evolution of anisotropy. J. Geophys. Res. (in prep).

Hess, H., 1964. Seismic anisotropy of hte uppermost mantle under oceans. Nature (London) 203, 629.

Higgie, K., Tommasi, A., 2012. Feedbacks between deformation and melt distribuion in the crust–mantle transition zone of the Oman ophiolite. Earth Planet. Sci. Lett. 359–360, 61–72.

Hill, R., 1952. The elastic behaviour of a crystalline aggregate. Proc. Phys. Soc. London, Sect. A 65, 349.

Hirth, G., Kohlstedt, D.L., 2003. Rheology of the upper mantle and the mantle wedge: a view from the experimentalists, inside the subduction factory. American Geophysical Union, Washington DC, pp. 83–105.

Holtzman, B.K., Kendall, J., 2010. Organized melt, seismic anisotropy, and plate boundary lubrication. Geochem. Geophys. Geosyst. 11.

Holtzman, B., Kohlstedt, D., Zimmerman, M., Heidelbach, F., Hiraga, T., Hustoft, J., 2003. Melt segregation and strain partitioning: implications for seismic anisotropy and mantle flow. Science 301, 1227–1230.

Ito, G., Dunn, R., Li, A., 2015. The origin of shear wave splitting beneath Iceland. Geophys. J. Int. 201, 1297–1312.

Jung, H., Karato, S.i., 2001. Water-induced fabric transitions in olivine. Science 293, 1460–1462.

Jung, H., Katayama, I., Jiang, Z., Hiraga, T., Karato, S., 2006. Effect of water and stress on the lattice-preferred orientation of olivine. Tectonophysics 421, 1–22. http://dx.doi.org/10.1016/j.tecto.2006.02.011.

Kaminski, E., Ribe, N.M., 2001. A kinematic model for recrystallization and texture development in olivine polycrystals. Earth Planet. Sci. Lett. 189, 253–267.

Kaminski, E., Ribe, N.M., 2002. Timescales for the evolution of seismic anisotropy in mantle flow. American Geophysical Union and The Geochemical Society, United States, p. 17.

Kaminski, É., Ribe, N.M., Browaeys, J.T., 2004. D-Rex, a program for calculation of seismic anisotropy due to crystal lattice preferred orientation in the convective upper mantle. Geophys. J. Int. 158, 744–752. http://dx.doi.org/10.1111/j.1365-246X.2004.02308.x.

Karato, S.i., 1987. Seismic anisotropy due to lattice preferred orientation of minerals; kinematic or dynamic? In: Manghnani, M.H., Syono, Y. (Eds.), High-pressure research in mineral physics. American Geophysical Union, Washington, DC, United States, pp. 455–471

Karato, S.i., 1988. The role of recrystallization in the preferred orientation of olivine. In: Babuska, V., Plomerova, J., Cerveny, V., Liebermann, R.C. (Eds.), Anisotropy and inhomogeneity of the lithosphere and asthenosphere. Elsevier, Amsterdam, Netherlands, pp. 107–122.

Karato, S.-i., Jung, H., Katayama, I., Skemer, P., 2008. Geodynamic significance of seismic anisotropy of the upper mantle: new insights from laboratory studies. Annu. Rev. Earth Planet. Sci. 59–95.

Katayama, I., Jung, H., Karato, S.-i., 2004. New type of olivine fabric from deformation experiments at modest water content and low stress. Geology 32, 1045. http://dx.doi.org/10.1130/g20805.1.

Klíma, K., Babuška, V., 1968. A comparison of measured and calculated elastic anisotropies of marble. Stud. Geophys. Geod. 12, 377–384.

Kneller, E., van Keken, P., Karato, S.-i., 2005. B-type fabric in the mantle wedge: Insights from high-resolution non-Newtonian subduction zone models. Earth Planet. Sci. Lett. 237, 781–797.

Knoll, M., Tommasi, A., Logé, R.E., Signorelli, J.W., 2009. A multiscale approach to model the anisotropic deformation of lithospheric plates. Geochem. Geophys. Geosyst. 10.

Komatitsch, D., Tromp, J., 1999. Introduction to the spectral element method for three-dimensional seismic wave propagation. Geophys. J. Int. 139, 806–822.

Laske, G., Masters, G., 1998. Surface-wave polarization data and global anisotropic structure. Geophys. J. Int. 132, 508–520.

Lassak, T.M., Fouch, M.J., Hall, C.E., Kaminski, É., 2006. Seismic characterization of mantle flow in subduction systems: can we resolve a hydrated mantle wedge? Earth Planet. Sci. Lett. 243, 632–649. http://dx.doi.org/10.1016/j.epsl.2006.01.022.

Li, Z.H., Di Leo, J.F., Ribe, N.M., 2014. Subduction-induced mantle flow, finite strain, and seismic anisotropy: numerical modeling. J. Geophys. Res. Solid Earth 119, 5052–5076.

Long, M.D., Becker, T.W., 2010. Mantle dynamics and seismic anisotropy. Earth Planet. Sci. Lett. 297, 341–354.

Long, M.D., Silver, P.G., 2009. Shear wave splitting and mantle anisotropy: measurements, interpretations, and new directions. Surv. Geophys. 30, 407–461. http://dx.doi.org/10.1007/s10712-009-9075-1.

Love, A., 1927. The mathematical theory of elasticity.

Mainprice, D., 2015. Seismic anisotropy of the deep Earth from a mineral and rock physics perspective. 2nd edition. Treatese of Geophysics vol. 2 pp. 437–491.

Mainprice, D., Silver, P.G., 1993. Interpretation of SKS-waves using samples from the subcontinental lithosphere. In: Mainprice, D., Vauchez, A., Montagner, J.P. (Eds.), Dynamics of the subcontinental mantle; from seismic anisotropy to mountain building. Elsevier, Amsterdam, Netherlands, pp. 257–280.

Mainprice, D., Hielscher, R., Schaeben, H., 2011. Calculating anisotropic physical properties from texture data using the MTEX open-source package. Geol. Soc. Lond. Spec. Publ. 360, 175–192.

Mainprice, D., Bachmann, F., Hielscher, R., Schaeben, H., 2014. Descriptive tools for the analysis of texture projects with large datasets using MTEX: strength, symmetry and components. Geol. Soc. Lond. Spec. Publ. 409 (SP409. 408).

Mei, S., Suzuki, A.M., Kohlstedt, D.L., Dixon, N.A., Durham, W.B., 2010. Experimental constraints on the strength of the lithospheric mantle. J. Geophys. Res. 115. http://dx.doi.org/10.1029/2009jb006873.

Mercier, J.C., Nicolas, A., 1975. Textures and fabrics of upper-mantle peridotites as illustrated by xenoliths from basalts. J. Petrol. 16, 454–487.

Miyazaki, T., Sueyoshi, K., Hiraga, T., 2013. Olivine crystals align during diffusion creep of Earth's upper mantle. Nature 502, 321–326.

Montagner, J.P., Nataf, H.C., 1986. A simple method for inverting the azimuthal anisotropy of surface waves. J. Geophys. Res. Solid Earth 91 (1978–2012), 511–520.

Montagner, J.P., Tanimoto, T., 1991. Global upper mantle tomography of seismic velocities and anisotropies. J. Geophys. Res. Solid Earth 96, 20337–20351.

Montagner, J.P., Griot-Pommera, D.A., Lavé, J., 2000. How to relate body wave and surface wave anisotropy? J. Geophys. Res. Solid Earth 105 (1978–2012), 19015–19027.

Nettles, M., Dziewoński, A.M., 2008. Radially anisotropic shear velocity structure of the upper mantle globally and beneath North America. J. Geophys. Res. Solid Earth 1978–2012, 113.

Nicolas, A., Christensen, N.I., 1987. Formation of anisotropy in upper mantle peridotites; a review. In: Fuchs, K., Froidevaux, C. (Eds.), Composition, structure and dynamics of the lithosphere–asthenosphere system. American Geophysical Union, Washington, DC, United States, pp. 111–123.

Nicolas, A., Bouchez, J.L., Boudier, F., Mercier, J.C., 1971. Textures, structures and fabrics due to solid state flow in some European lherzolites. Tectonophysics 12, 55–86.

Nicolas, A., Boudier, F., Boullier, A.M., 1973. Mechanisms of flow in naturally and experimentally deformed peridotites. Am. J. Sci. 273, 853–876.

Niehuesbernd, J., Müller, C., Pantleon, W., Bruder, E., 2013. Quantification of local and global elastic anisotropy in ultrafine grained gradient microstructures, produced by linear flow splitting. Mater. Sci. Eng. A 560, 273–277.

Nishimura, C.E., Forsyth, D.W., 1989. The anisotropic structure of the upper mantle in the Pacific. Geophys. J. Int. 96, 203–229.

Panning, M., Romanowicz, B., 2006. A three-dimensional radially anisotropic model of shear velocity in the whole mantle. Geophys. J. Int. 167, 361–379. http://dx.doi.org/10.1111/j.1365-246X.2006.03100.x.

Paterson, M.S., Olgaard, D.L., 2000. Rock deformation tests to large shear strains in torsion. J. Struct. Geol. 22, 1341–1358.

Peselnick, L., Nicolas, A., Stevenson, P., 1974. Velocity anisotropy in a mantle peridotite from the Ivrea Zone: application to upper mantle anisotropy. J. Geophys. Res. 79, 1175–1182.

Prior, D.J., Boyle, A.P., Brenker, F., Cheadle, M.C., Day, A., Lopez, G., Peruzzi, L., Potts, G., Reddy, S., Spiess, R., Timms, N.E., Trimby, P., Wheeler, J., Zetterstrom, L., 1999. The application of electron backscatter diffraction and orientation contrast imaging in the SEM to textural problems in rocks. Am. Mineral. 84, 1741–1759.

Raitt, R.W., 1963. Seismic refration studies of the Mendicino fracture zone. Abstract of Papers 6. International Association of Physical Oceanography.

Raleigh, C.B., 1963. Fabrics of naturally and experimentally deformed olivine. UCLA.

Raleigh, C.B., 1965. Structure and petrology of an alpine peridotite on Cypress Island, Washington, U.S.A. Beitr. Mineral. Petrol. 11, 719–741.
Raleigh, C., 1968. Mechanisms of plastic deformation of olivine. J. Geophys. Res. 73, 5391–5406.
Raterron, P., Amiguet, E., Chen, J., Li, L., Cordier, P., 2009. Experimental deformation of olivine single crystals at mantle pressures and temperatures. Phys. Earth Planet. Inter. 172, 74–83. http://dx.doi.org/10.1016/j.pepi.2008.07.026.
Ribe, N.M., Yu, Y., 1991. A theory for plastic deformation and textural evolution of olivine polycrystals. J. Geophys. Res. B Solid Earth Planets 96, 8325–8335.
Schoenberg, M., Muir, F., 1989. A calculus for finely layered anisotropic media. Geophysics 54, 581–589.
Schulte-Pelkum, V., Blackman, D.K., 2003. A synthesis of seismic P and S anisotropy. Geophys. J. Int. 154, 166–178.
Seront, B., Mainprice, D., Christensen, N.I., 1993. A determination of the three-dimensional seismic properties of anorthosite: comparison between values calculated from the petrofabric and direct laboratory measurements. J. Geophys. Res. 98, 2209–2221.
Shapiro, N., Ritzwoller, M., 2002. Monte-Carlo inversion for a global shear-velocity model of the crust and upper mantle. Geophys. J. Int. 151, 88–105.
Shor, G.G., Pollard, D.D., 1964. Mohole site selection studies north of Maui. J. Geophys. Res. 69, 1627–1637.
Signorelli, J., Tommasi, A., 2015. Modeling the effect of subgrain rotation recrystallization on the evolution of olivine crystal preferred orientations in simple shear. Earth Planet. Sci. Lett. 430, 356–366.
Silver, P.G., Savage, M.K., 1994. The interpretation of shear-wave splitting parameters in the presence of 2 anisotropic layers. Geophys. J. Int. 119, 949–963.
Skemer, P., Karato, S., 2008. Sheared lherzolite xenoliths revisited. J. Geophys. Res. 113, B07205. http://dx.doi.org/10.1029/2007JB005286.
Skemer, P., Katayama, B., Jiang, Z.T., Karato, S., 2005. The misorientation index: development of a new method for calculating the strength of lattice-preferred orientation. Tectonophysics 411, 157–167. http://dx.doi.org/10.1016/j.tecto.2005.08.023.
Skemer, P., Warren, J.M., Kelemen, P.B., Hirth, G., 2010. Microstructural and rheological evolution of a mantle shear zone. J. Petrol. 51, 43–53. http://dx.doi.org/10.1093/petrology/egp057.
Skemer, P., Sundberg, M., Hirth, G., Cooper, R., 2011. Torsion experiments on coarse-grained dunite: implications for microstructural evolution when diffusion creep is suppressed. Geol. Soc. Lond. Spec. Publ. 360, 211–223. http://dx.doi.org/10.1144/sp360.12.
Skemer, P., Warren, J.M., Hirth, G., 2012. The influence of deformation history on the interpretation of seismic anisotropy. Geochem. Geophys. Geosyst. 13. http://dx.doi.org/10.1029/2011GC003988.
Song, T.R.A., Kawakatsu, H., 2012. Subduction of oceanic asthenosphere: evidence from sub-slab seismic anisotropy. Geophys. Res. Lett. 39.
Soustelle, V., Tommasi, A., Demouchy, S., Ionov, D., 2010. Deformation and fluid–rock interaction in the supra-subduction mantle: microstructures and water contents in peridotite xenoliths from the Avacha Volcano, Kamchatka. J. Petrol. 51, 363–394.
Sundberg, M., Cooper, R.F., 2008. Crystallographic preferred orientation produced by diffusional creep of harzburgite: effects of chemical interactions among phases during plastic flow. J. Geophys. Res. Solid Earth 1978–2012, 113.
Takeuchi, H., Saito, M., 1972. Seismic surface waves. Methods Comput. Phys. 11, 217–295.
Tanimoto, T., Anderson, D.L., 1984. Mapping convection in the mantle. Geophys. Res. Lett. 11, 287–290.
Tanimoto, T., Anderson, D.L., 1985. Lateral heterogeneity and azimuthal anisotropy of the upper mantle — love and Rayleigh-waves 100–250 S. J. Geophys. Res. Solid Earth Planets 90, 1842–1858.
Tatham, D., Lloyd, G., Butler, R., Casey, M., 2008. Amphibole and lower crustal seismic properties. Earth Planet. Sci. Lett. 267, 118–128.
Tommasi, A., 1998. Forward modeling of the development of seismic anisotropy in the upper mantle. Earth Planet. Sci. Lett. 160, 1–13.
Tommasi, A., Mainprice, D., Canova, G., Chastel, Y., 2000. Viscoplastic self-consistent and equilibrium-based modeling of olivine lattice preferred orientations; implications for the upper mantle seismic anisotropy. J. Geophys. Res. B Solid Earth Planets 105, 7893–7908.
Turner, F.J., 1942. Preferred orientation of olivine crystals in peridotites, with special reference to New Zealand examples. Trans. Roy. Soc. NZ 72, 280–300.
Turner, F.J., Weiss, L.E., 1963. Structural analysis of metamorphic tectonites.
Van der Wal, D., Chopra, P., Drury, M., Gerald, J.F., 1993. Relationships between dynamically recrystallized grain size and deformation conditions in experimentally deformed olivine rocks. Geophys. Res. Lett. 20, 1479–1482.
Verma, R.K., 1960. Elasticity of some high-density crystals. J. Geophys. Res. 65, 757–766.
Vollmer, F.W., 1990. An application of eigenvalue methods to structural domain analysis. Geol. Soc. Am. Bull. 102, 786–791.
Walker, A.M., Wookey, J., 2012. MSAT—a new toolkit for the analysis of elastic and seismic anisotropy. Comput. Geosci. 49, 81–90.
Wallis, S., Kobayashi, H., Nishii, A., Mizukami, T., Seto, Y., 2011. Obliteration of olivine crystallographic preferred orientation patterns in subduction-related antigorite-bearing mantle peridotite: an example from the Higashi–Akaishi body, SW Japan. Geol. Soc. Lond. Spec. Publ. 360, 113–127.
Wang, Y., Durham, W.B., Getting, I.C., Weidner, D.J., 2003. The deformation-DIA: a new apparatus for high temperature triaxial deformation to pressures up to 15 GPa. Rev. Sci. Instrum. 74, 3002–3011.
Warren, J.M., Hirth, G., 2006. Grain size sensitive deformation mechanisms in naturally deformed peridotites. Earth Planet. Sci. Lett. 248, 438–450.
Warren, J.M., Hirth, G., Kelemen, P., 2008. Evolution of lattice-preferred orientation during simple shear in the mantle. Earth Planet. Sci. Lett. 272, 501–512.
Webber, C., Newman, J., Holyoke, C.W., Little, T., Tikoff, B., 2010. Fabric development in cm-scale shear zones in ultramafic rocks, Red Hills, New Zealand. Tectonophysics 489, 55–75. http://dx.doi.org/10.1016/j.tecto.2010.04.001.
Wenk, H.-R., Tomé, C.N., 1999. Modeling dynamic recrystallization of olivine aggregates deformed in simple shear. J. Geophys. Res. 104, 25513–25527.
Wenk, H.R., Bennett, K., Canova, G.R., Molinari, A., 1991. Modeling plastic-deformation of peridotite with the self-consistent theory. J. Geophys. Res. Solid Earth Planets 96, 8337–8349.
Wheeler, J., 2009. The preservation of seismic anisotropy in the Earth's mantle during diffusion creep. Geophys. J. Int. 178, 1723–1732.
Wolfe, C.J., Solomon, S.C., 1998. Shear-wave splitting and implications for mantle flow beneath the MELT region of the East Pacific Rise. Science 280, 1230–1232.
Yamazaki, D., Karato, S.-i., 2001. High-pressure rotational deformation apparatus to 15 GPa. Rev. Sci. Instrum. 72, 4207. http://dx.doi.org/10.1063/1.1412858.
Yuan, H., Romanowicz, B., 2010. Lithospheric layering in the North American craton. Nature 466, 1063–1068.
Zhang, S., Karato, S.i., 1995. Lattice preferred orientation of olivine aggregates deformed in simple shear. Nature (London) 375, 774–777.
Zhang, S., Karato, S.i., Fitz, G.J., Faul, U.H., Zhou, Y., 2000. Simple shear deformation of olivine aggregates. Tectonophysics 316, 133–152.
Zhong, X., Frehner, M., Kunze, K., Zappone, A., 2014. A novel EBSD-based finite-element wave propagation model for investigating seismic anisotropy: Application to Finero Peridotite, Ivrea-Verbano Zone, Northern Italy. Geophys. Res. Lett. 41, 7105–7114.
Zietlow, D.W., Sheehan, A.F., Molnar, P.H., Savage, M.K., Hirth, G., Collins, J.A., Hager, B.H., 2014. Upper mantle seismic anisotropy at a strike-slip boundary: South Island, New Zealand. J. Geophys. Res. Solid Earth 119, 1020–1040.